An Infrared Picosecond Optical Parametric Oscillator for Polymer Ablation

Peter Smythe

A thesis submitted for the degree of
Bachelor of Science, Honours
The Australian National University

October, 2004

Declaration

This thesis is an account of research undertaken between February 2003 and October 2003 at The Laser Physics Centre, Research School of Physical Sciences and Engineering, The Australian National University, Canberra, Australia.

Except where acknowledged in the customary manner, the material presented in this thesis is, to the best of my knowledge, original and has not been submitted in whole or part for a degree in any university.

Peter Smythe
October, 2004

Acknowledgements

I would like to thank everyone who has contributed to what has been a thoroughly enjoyable year.

Firstly, I would like to thank Prof. Barry Luther-Davies for his supervision this year. I am grateful for all the time and work that Barry has injected into this project. His approach to work, and enthusiasm in the lab are motivational. I feel very fortunate and grateful for having had such a great supervisor.

Thank you to all of the members of the Laser Physics Centre for their assistance and for making it such a great place to work. I offer special thanks Vesselin Kolev and Khu Vu, for all of their help. Their assistance throughout the year was invaluable.

Thanks to all of the honours students for making it such an entertaining year, especially on Fridays.

Above all, I am deeply grateful to my family, who have always supported, encouraged, and inspired me through everything I've done.

Abstract

The development of an infrared optical parametric oscillator based on Magnesium Oxide doped Periodically Poled Lithium Niobate (MgO:PPLN) is described. The OPO is synchronously pumped by a high average power, picosecond, Nd:YVO_4 mode-locked laser operating at 1064nm. The OPO generates signal and idler radiation at wavelengths centered at 1550nm and 3.4μm respectively. The OPO is singly resonant at the the signal wavelength.

The multiple QPM grating periods and temperature control imposed upon the PPLN crystal afford a broad tuning range of the OPO output. The signal is tunable from 1450-1700nm, corresponding to an idler tuning range of 2.8-4.0μm. Pumping the OPO at 10W yielded 1.5W of extracted idler power at 3.3μm.

The OPO is intended as a light source for pulsed laser ablation of polymers. Previous demonstrations of pulsed laser polymer ablation used a Free Electron Laser as the light source. The OPO was successfully used to evaporate polymers, although the physical mechanism is uncertain. Further development of this, or similar devices offers a flexible, and more accessible alternative to a FEL for polymer ablation.

Contents

List of Figures

List of Tables

Introduction

1.1 Motivation

The production of high quality thin polymer films is becoming increasingly important in the development of novel devices. Applications in organic-optoelectronics [1, 2, 3], optical waveguides [4], biomedical engineering [5], chemical and biological sensing [6] amongst other fields, require polymeric films of precisely controlled chemical and structural properties, thickness, and surface roughness. Thus, the development of thin film deposition techniques, suitable for the formation of polymeric films is highly desirable.

Currently, thin films of polymeric material are synthesised using various techniques of differing complexity and quality. The suitability of a particular technique to a specific problem depends on the properties of the materials and the required tolerances of the film properties. Currently, the simplest methods for the deposition of thin organic films are spin coating, drop casting, aerosol spray and ink-jet deposition [7]. In these deposition techniques, the solid material is dissolved in a volatile solvent which is subsequently dispersed on the substrate surface. The thin polymer film remains after the solvent evaporates [8]. It is difficult however, to precisely control film thickness and uniformity, using such methods. Vapour phase deposition processes provide an attractive alternative, and offer the potential for improved control of film thickness and surface texture.

Physical vapour phase deposition techniques are a common means of depositing films on a substrate and are widely used for inorganic materials. Physical Vapour Deposition techniques involve the deposition of materials directly from a the vapour phase thus avoiding problems associated with solvents which occur in chemical vapour deposition. The vapour phase is created by giving molecules sufficient energy to overcome the intermolecular bond energy and thus liberating them from the bulk material, generally by means of heating, or bombardment by electron- or ion-beams. Ideally, the physical polymer vapour exists with the same chemical structure as the bulk target material. The major problem encountered when applying such techniques to polymers is the creation of a polymer vapour without altering the chemical or structural composition (with respect to the bulk material).

Thermal and electron beam evaporation involve the heating of a target material, causing evaporation into the vapour phase. These techniques are not suitable for use with polymers as the polymer chains have a propensity to fragment into monomers or oligomers. These monomers will not (in general) recombine upon condensation on the substrate, and hence this is an unsatisfactory method for the creation of polymeric films of well controlled composition and molecular weight distribution.

Pulsed Laser Deposition (PLD) is a physical vapour deposition technique that relies on the ablation of material from a solid target to produce a vapour. A high power, pulsed laser is focused onto a target area of the solid evaporant material. The high local heating

rate of a small surface layer causes the material to evaporate. The ablated material rapidly expands into the vacuum chamber and is free to deposit on a substrate. PLD is a valuable technique as the stoichiometry and molecular weight distribution can be retained in the deposited films, with respect to the bulk target material [9]. This is imperative for the creation of polymer films and hence, this approach was pursued as the objective for this project.

Two principle categories of Pulsed Laser Ablation of polymers are reported in the literature, distinguished by the region of the electromagnetic spectrum at which the laser operates. Ultraviolet PLD has enjoyed limited success in polymeric film growth in those cases where depolymerisation can occur at the target surface and repolymerisation occurs upon contact with the substrate [10, 11, 12]. In general however, the photon energy is greater than the energy required to bond individual monomers into the polymer chain, leading to the decomposition of the polymer into monomeric units, which are the primary ablation product, making this method largely unsuitable for polymeric film synthesis [13].

To avoid decomposition of polymers during ablation, the photon energy is reduced by moving into the infrared spectral region. Resonant infrared pulsed-laser deposition (RIR-PLD) has been used to successfully grow organic films [5, 9]. This method involves excitation of vibrational resonances of particular bonds in the polymer, leading to the liberation of complete polymer chains into the vapour phase. These excitations correspond to strong absorption peaks in the target polymer's IR absorption spectrum, which can be indexed to particular vibrational modes of specific bonds. These absorption peaks are present in all organic materials, and hence this technique promises to be useful for a vast range of polymers.

A high power laser, tunable over the mid infrared region is required for RIR-PLD. Conventional solid-state, dye and gas lasers have proven to be unsuitable light sources for RIR-PLD as they do not operate at appropriate frequencies or are not tunable over a suitable range. Experiments using a Free Electron Laser (FEL) have successfully implemented this polymer deposition scheme [5]. The aim of this project is to develop a high power Optical Parametric Oscillator as an alternative light source for pulsed laser ablation of polymers.

1.2 Pulsed Laser Deposition

Pulsed Laser Deposition is a method of thin film growth involving the ablation of a solid target into a vapour phase and its subsequent condensation onto a substrate. This procedure must be carried out in high vacuum, to allow the free expansion of the vapour plume. PLD has proven successful in depositing uniform thin films of complex structure and stoichiometry such as superconducting oxides [14] and more recently polymers [5], which had not been achieved using other deposition techniques.

The greatest challenge in vapour deposition of polymers is the coupling of sufficient energy into individual excitations to overcome the intermolecular forces without causing depolymerisation [9]. The principal difference between PLD and other physical vapour deposition techniques is the mechanism by which material is removed from the target, and the vapour phase of the evaporant (target material) is formed.

Conventional pulsed laser deposition using an ultraviolet laser as the energy source is generally destructive of organic targets [13, 15]. The ablation process in UV PLD is initiated by strong, non-specific electronic excitations. This energy couples to lattice excitations, increasing the thermal energy and consequently heating the target to its evap-

oration temperature. Observations of polymer films deposited film using UV PLD reveal fragmentation of the target polymer through photothermal or photochemical means [9].

The success of Resonant Infrared Pulsed-Laser Deposition (RIR-PLD) of polymers is a result of the different physical mechanism responsible for the coupling of energy from the laser mode to the target. In RIR-PLD, the frequency of the IR laser (or in our case OPO) source is tuned to correspond to a vibrational resonance of the target polymer. The particular excitation mode usually relates to end groups responsible for hydrogen bonding or pendant functional groups which have strong dipole-dipole interactions, as opposed to backbone modes [9]. Theoretical analysis of RIR-PLD suggests that explicitly controlling the flow of energy into the target material via vibrational excitations allows vaporisation of the polymer without altering its structural and chemical composition [16]. Qualitatively, this can be thought of as shaking entire polymer chains free from the solid phase.

Computational modeling of laser-matter interactions has resulted in the most thorough theoretical analysis of the problem to date. Molecular-dynamics based computer simulations of the interaction of pulsed, coherent mid-infrared radiation with organic molecules in the bulk, have provided a model consistent with experimental observations [17].

The laser light acts only upon molecules within a small target volume defined by the laser spot size and the penetration depth into the material. For the duration of the laser pulse, the internal energy of molecules within this volume increases due to excitation of a particular vibrational mode. This energy rapidly transfers to thermal energy, increasing the temperature of the target volume on the time scale of the pulse duration (10-20ps). The severe heating rate exceeds the thermal expansion rate of the material, resulting in localised build up of high pressure. This pressure results in forces acting normal to the material surface which cause the ejection of the top molecular layers into the vapour phase.

In addition, the intense heating caused by the short laser pulse results in strong compressive pressures, which inhibits the melting phase transition, allowing superheating of the material. This causes a rapid phase transition at elevated temperatures directly from the solid to vapour phase, which is homogenous throughout the irradiated volume. This physical phenomenon is known as a phase explosion or homogenous explosive boiling and is consistent with experimental observations.

The ejected material, a mixture of vapour and small liquid droplets expands adiabatically in the vacuum chamber. The dynamics of the vapour plume have also been modelled via computer simulations [18] but will not be discussed here. The vapour condenses on the substrate upon contact, producing a uniform film with low surface roughness, and more importantly, with the same structural chemistry, molecular weight distribution and physical properties of the bulk target polymer.

1.3 Optical Parametric Oscillators

Optical Parametric Oscillators are resonant devices that output continuously tuneable coherent radiation. An Optical Parametric Oscillator (OPO) consists of a nonlinear medium, enclosed in a resonant cavity which when pumped by a laser, provides gain at new frequencies via a stimulated parametric process. The gain material is contained within a resonant cavity to provide optical feedback at these frequencies. Figure 1.1 is a schematic of a simplified OPO. Such a device operated in a single-pass configuration (no cavity) is known as an Optical Parametric Amplifier (OPA).

In an OPA, a *pump* laser beam is incident upon a non-linear optical material with a strong second order response. A single photon from the pump laser will spontaneously

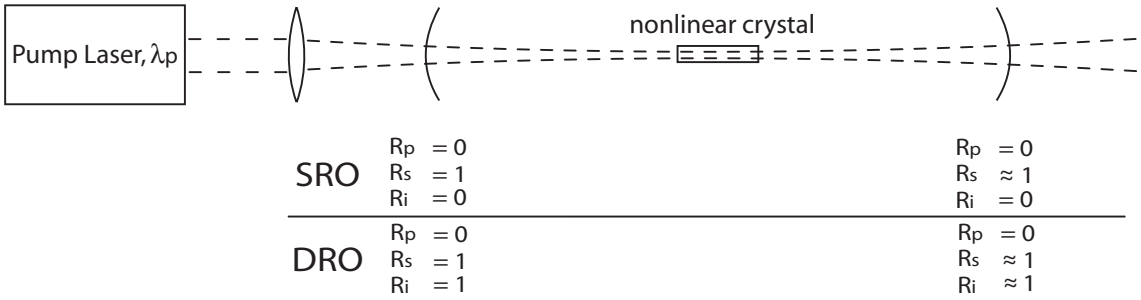

Figure 1.1: Schematic of a simple Optical Parametric Oscillator. The reflectivities of the cavity mirrors are shown for a singly resonant (SRO) and doubly resonant (DRO) oscillator.

decay into a pair of lower energy photons, a mechanism known as parametric fluorescence. These photons are known as the *signal* and *idler* photons, where by convention the signal is of higher frequency than the idler. The conservation of photon energy during the interaction imposes an equivalent condition on the frequencies, as in Equation 1.1.

$$\omega_p = \omega_s + \omega_i \tag{1.1}$$

where ω_p, ω_s, and ω_i are the frequencies of the pump, signal and idler photons respectively. The nonlinear polarization allows mixing to occur between the pump and the generated signal (and idler) photons, cyclically generating more idler (and signal) photons respectively, continuously drawing energy from the pump beam.

In a nonlinear medium, the polarisation is still dominated by the linear term, which is several orders of magnitude stronger than the second order polarization. To observe macroscopic nonlinear optical effects, it is therefore essential that waves generated in different spatial regions in the medium add coherently. This demands that the generated waves and the source polarisation have equal phase velocities in the medium (the source polarisation is driven by the pump wave). This criterion is known as the phase matching condition and is equivalent (through multiplication by $\hbar$) to linear momentum conservation, as is evident in Equation 1.2.

$$\mathbf{k_p} = \mathbf{k_s} + \mathbf{k_i} \tag{1.2}$$

where the wave vector is defined $k_j = n_j\omega_j/c$, the refractive index n_j is a frequency dependent function, defined at ω_j, and c is the speed of light propagating in free space. It is important to note that the energy conservation condition Equation 1.1, does not predict a unique pair of signal and idler frequencies for a given pump frequency [19]. It is the requirement that both the phase matching and energy conservation conditions are simultaneously satisfied which leads to the output of a pair of photons with distinct, predictable frequencies.

Energy and momentum conservation (that is Equations 1.1 and 1.2) are not in general, simultaneously satisfied, due to material dispersion. The refractive indices at the pump, signal and idler frequencies are not equal in general ($n_p \neq n_s \neq n_i$). This is made clear by Equation 1.3, which provides an equivalent condition to the conservation of linear momentum described by Equation 1.2.

$$n_p w_p = n_s w_s + n_i w_i \tag{1.3}$$

The wave vector mismatch resulting from the effects of group velocity dispersion is defined as $\Delta k = k_p - k_s - k_i$

Exploiting the properties of birefringent materials however, it is possible to phase match such a system by choosing appropriate polarisations and propagation directions for the source and generated waves. The system can be phase matched by tuning the angle of the crystal and hence the propagation direction with respect to the optical axis, a technique known as Angle Tuning. This technique however, is limited by the birefringent properties of the material and consequently cannot be used to phase match all interactions.

Periodically inverting the sign of the driving non-linear polarization is another common phase matching technique. This can be achieved by introducing a crystal in which the sign of the susceptibility tensor is inverted periodically, introducing an additional phase parameter, the grating vector k_g, to compensate the phase mismatch such that $\Delta k = 0$. This technique is known as periodic poling, an example of quasi-phase matching (QPM).

Quasi-phase matching is not limited by the inherent optical properties of the crystal (providing the material is transparent at appropriate frequencies) and is dependent only on the grating period, making it possible in principle to phase match any nonlinear interaction. Periodic poling is convenient, as phase matching is dependent on an artificial parameter, the poling period, and not the physical properties of the crystal. Electric field poling can be used to manufacture gratings in ferroelectric materials to the specifications required to phase match a particular interaction. Furthermore, as the optical anisotropy of the material is not required to phase match the system, the propagation direction can be chosen purely to maximise the effective nonlinearity.

The proposed OPO will convert a pump wave at 1064nm to a signal wave at 1550nm and an idler wave at $3.4\mu m$. The idler wave will be used to as the light source for resonant infrared pulsed laser ablation of polymers. Crystalline MgO:$LiNbO_3$ is a suitable material for periodic poling due to its strong second order nonlinearity, and low absorption at the proposed pump, signal and idler frequencies. MgO:$LiNb0_3$ has a transparency window extending to $5\mu m$, making it suitable for the long idler wavelength. The material's high photorefractive damage threshold is also of importance, as it will be used as the gain medium in a high power device. The crystal chosen for this project was a commercially available Periodically Poled Magnesium Oxide doped Lithium Niobate (MgO:PPLN) crystal, containing six different grating periods. These periods allow course tuning of the generated frequencies, whilst temperature control of the crystal allows continuous tuning of the grating period and hence the signal and idler frequencies.

The OPO will be synchronously pumped by a high average-power, mode-locked Nd:YVO_4 laser, operating at 1064nm with picosecond pulse duration. The reflectivity of the cavity mirrors are such that only one of the generated waves, the shorter wavelength signal, is resonant.

Chapter 2: Introduction to NLO

2.1 Introduction to Nonlinear Optics

All optical effects, linear or nonlinear are caused by the interaction of electromagnetic radiation with matter . An electric (optical) field propagating through a dielectric material induces a macroscopic polarisation, the nature of this response falling broadly into two categories. In linear optics, the induced polarisation is proportional to the electric field at that point, related by Equation 2.1.

$$\mathbf{P} = \epsilon_0 \boldsymbol{\chi_1} \cdot \mathbf{E} \tag{2.1}$$

where χ_1, the linear susceptibility is a characteristic property of the medium. This linear response of the material forms the realm of conventional, linear optics, operating at low field intensities, where the electric susceptibility $\boldsymbol{\chi}$ is field independent.

The realisation of the laser provided experimentalists with a new light source, many orders of magnitude brighter than those previously available. At high fields, the field dependence of the electric susceptibility is no longer negligible, and a deviation from a linear response is observed. The principle of causality implies that the induced polarisation, and hence the electric susceptibility are functions of the electric field . Expanding these relationships in terms that are directly proportional to increasing powers of the applied field,

$$\chi(E) = \chi_{\mathbf{1}} + \chi_{\mathbf{2}} \cdot \mathbf{E} + \chi_{\mathbf{3}} \vdots \mathbf{EE} + \dots \tag{2.2}$$

$$P = \epsilon_0 \chi_{\mathbf{1}} \cdot \mathbf{E} + \epsilon_0 \chi_{\mathbf{2}} \vdots \mathbf{EE} + \epsilon_0 \chi_{\mathbf{3}} \vdots \mathbf{EEE} + \dots \tag{2.3}$$

where $\boldsymbol{\chi_2}$ and $\boldsymbol{\chi_3}$ are the second and third order nonlinear susceptibility tensors respectively. The ratio of consecutive order terms is of the same magnitude as the ratio of the applied field to the atomic field strength [20], necessitating high field intensities to observe higher order effects. Many interesting physical phenomena arise from these higher order responses, prompting both fundamental scientific and application-driven investigations.

The nonlinear polarisation terms act as the source terms for emitted electromagnetic radiation.

2.1.1 Origin of Optical Nonlinearity

The susceptibility $\boldsymbol{\chi}$ relates the induced polarisation response of a material to an applied electric field. This macroscopic response represents the net dipole moment per unit volume

of the material, corresponding to a sum of the dipole moments of all the atoms and molecules on the microscopic scale. The physical origin of the nonlinear polarisation must therefore be discussed in terms of the microscopic structure of the medium. This can only be evaluated properly by a full quantum mechanical treatment. Simpler models however, can be used to phenomenologically describe the origin of the optical nonlinearity.

A simple classical model describes the material as a density distribution (N per unit volume) of classical anharmonic oscillators [20, 19, 21]. The oscillator represents an electron bound to a core (electronic excitations), or an infrared-active molecular vibration . This model is represented in Figure 2.1 where it can be seen that the potential energy of the oscillator $V(x)$ is not quite a quadratic function of the deviation from the equilibrium position, due to a nonlinear spring constant (describing the nonlinear polarisation response of the nonlinear optical material). The optical field with Fourier components at frequencies ω_1 and ω_2 is the driving term for the oscillator as described in Equation 2.4.

$$\frac{d^2x}{dt^2} + \Gamma\frac{dx}{dt} + \omega_0^2 x + ax^2 = \frac{e}{2m}[E_1(e^{i\omega_1 t} + e^{-i\omega_1 t}) + E_2(e^{i\omega_2 t} + e^{-i\omega_2 t})] \tag{2.4}$$

where x is the spatial deviation from minimum potential as shown in Figure 2.1. Γ is the damping coefficient, and the anharmonic restoring force is given by max^2.

Assuming the anharmonic term is sufficiently small so that it can be treated as a perturbation, the first order and second order solutions can be obtained. These are summarised in Equations 2.5 and 2.6 [20].

$$x_{Lin} = x^{(1)}(\omega_1) + x^{(1)}(\omega_2) \tag{2.5}$$

$$x_{NL} = x^{(2)}(\omega_1 + \omega_2) + x^{(2)}(\omega_1 - \omega_2) + x^{(2)}(2\omega_1) + x^{(2)}(2\omega_2) + x^2(0) \tag{2.6}$$

Higher order solutions can be found but are not discussed here as the second order solution adequately demonstrates the generation of new frequencies through the nonlinear interaction. Here, x describes the field-induced separation of bound charges. The macroscopic polarisation induced by the driving electric field is simply the product of the volume density of oscillators, carried charge and its displacement from equilibrium, that is $\boldsymbol{P} = Nqx$. The first order solution, Equation 2.5, has terms only at the input frequencies as expected for a linear response. New frequency components are clearly present in the second-order solution, Equation 2.6. The polarisation fields oscillating at frequencies $\omega_1 \pm \omega_2, 2\omega_1$ and $2\omega_2$ act as source terms, generating electromagnetic radiation at these frequencies. These physical phenomena are known as sum and difference generation and second harmonic generation respectively. The d.c. component represents a small average polarisation known as optical rectification.

In this oscillator model, the magnitude of the higher-order response depends on the degree of anharmonicity. An extension of this model from one to three spatial dimensions requires that the material possess some crystalline structural asymmetry to produce the anharmonicity thus ensuring that the polarisation response is not identical under reversal of the electric field. Failing this, no second (or any other even power) order nonlinear effect will be observed. In terms of crystal classes, only those lacking inversion symmetry will have non-zero even power susceptibilities. All materials however, display third-order and higher odd powered nonlinear responses at sufficiently high fields.

The nonlinear susceptibility tensor of a particular crystal must obey the same symmetry relations as the crystals space group.

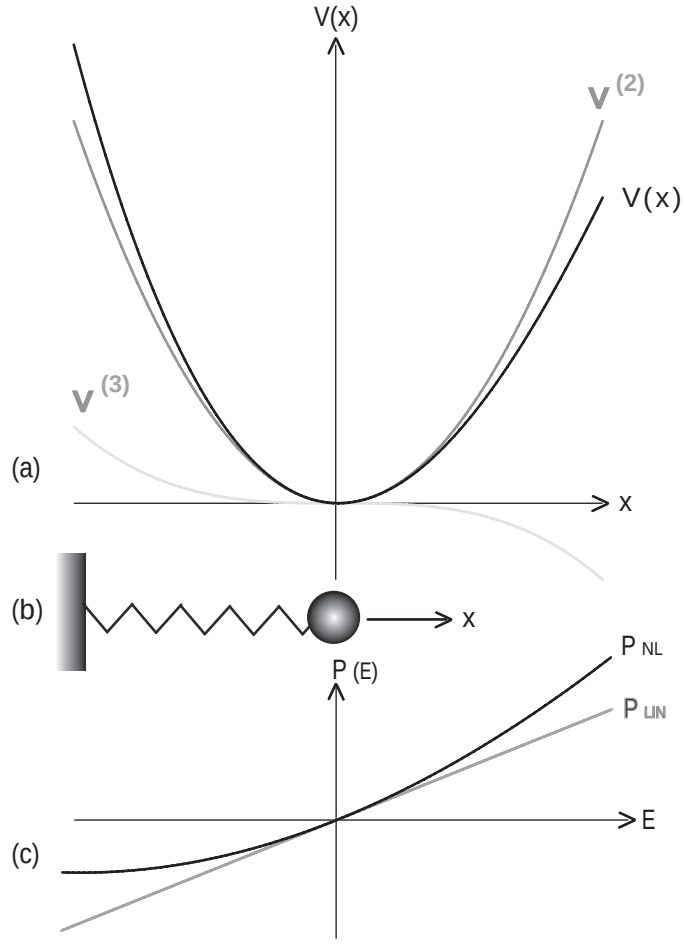

Figure 2.1: Anharmonic oscillator model of nonlinear susceptibilities. (a) Potential energy of the oscillator $V(x)$ as a function of the deviation from the equilibrium position x, as shown in (b). (c)Induced polarisation P_{NL} as a function of the optical field for a nonlinear medium. The deviation from a linear polarisation response P_{LIN} is clear.

2.1.2 Nonlinear Susceptibility

The nonlinear susceptibility must be described by a third rank tensor as a consequence of the vector nature of the $\boldsymbol{E}$ and $\boldsymbol{P}$ fields and the dependence on propagation direction. Two monochromatic electromagnetic waves can interact through the nonlinear polarisation of a dielectric, generating radiation at new frequencies. This can be demonstrated by an expansion into the Fourier components in Equation 2.6.

It is also instructive to consider the general form of the second-order nonlinear susceptibility.

$$P_i^{(2)} = \sum_{j,k} \epsilon_0 \chi_{ijk}^{(2)} E_j E_k \tag{2.7}$$

where i, j and k refer to orthogonal components in a Cartesian coordinate system. The second-order susceptibility tensor $\chi_{ijk}^{(2)}$, has in the general case, 27 (3^3) independent elements. As discussed in Section 2.1.2, second-order nonlinear effects occur due anharmonic oscillatory behavior of electrons caused by an asymmetric potential function. An asymmetric potential reflects asymmetry in the crystal structure and hence certain symmetry

conditions must be present if a material is to exhibit a second-order response. Crystals possessing a centre of symmetry induce symmetric polarisations under an $\boldsymbol{E}$ field reversal, hence only noncentrosymmetric crystals have a non-zero second-order susceptibility tensor. Additional symmetry relationships are imposed on the tensor by relations described by Armstrong [22] and Kleinman [23]. These relations stipulate that for a lossless (transparent) medium, no hysteresis exists in the relationship between $\boldsymbol{P}$ and $\boldsymbol{E}$ and hence P is a single valued function of $\boldsymbol{E}$. As a result, no physical significance can be attributed to the exchange of E_j and E_k, allowing a permutation relation on these indices. These indices can therefore be replaced by a single symbol, resulting in a contraction of the notation. [21] Equation 2.8 shows the resulting 3x6 tensor can be represented as a matrix, referred to as the Kleinman d-tensor which operates on the field.

$$\begin{pmatrix} P_1 \\ P_2 \\ P_3 \end{pmatrix} = \begin{pmatrix} d_{11} & d_{12} & d_{13} & d_{14} & d_{15} & d_{16} \\ d_{21} & d_{22} & d_{23} & d_{24} & d_{25} & d_{26} \\ d_{31} & d_{32} & d_{33} & d_{34} & d_{35} & d_{36} \end{pmatrix} \begin{pmatrix} E_x^2 \\ E_y^2 \\ E_z^2 \\ 2E_yE_z \\ 2E_xE_z \\ 2E_xE_y \end{pmatrix} \tag{2.8}$$

Here, the superfluous frequency subscripts have been contracted following the convention described in Equation 2.9, adopted from piezoelectric theory,

$$d_{ijk} \Rightarrow d_{im}, \quad \text{where} \quad i \in \begin{Bmatrix} x = 1 \\ y = 2 \\ z = 3 \end{Bmatrix}, \quad \text{and} \quad m \in \begin{Bmatrix} xx = 1 \\ yy = 2 \\ zz = 3 \\ yz = zy = 4 \\ xz = zx = 5 \\ xy = yx = 6 \end{Bmatrix} \tag{2.9}$$

Furthermore, for crystalline materials the contracted Kleinman tensor obeys the symmetry relations of the point symmetry group to which the crystal belongs.

It is also convenient to define a scalar quantity d_{eff} which describes the effective value of the nonlinear susceptibility, such that $d_{eff} = \chi^{(2)}_{eff}/2$. This single parameter describes the strength of the nonlinearity for any fixed geometry. The tensor components are defined with respect to the principle axis of the crystal, which need not concur with the (arbitrary) laboratory reference frame. The d_{eff} is thus a linear combination of all the tensor components with respect to the principle axis, and is dependent on propagation direction and the point symmetry group of the crystal. [24]

2.2 Coupled Wave Equations

The previous sections have been concerned with the nonlinear response of a medium to an applied electromagnetic field. The resulting nonlinear polarisation terms act as source terms for the generation of electromagnetic waves at new frequencies [25]. Maxwell's equations (Equations 2.10 and 2.11) describe all electromagnetic phenomena and will be used here to derive relationships between the driving nonlinear polarisation and the fields they generate.

$$\nabla \times E = -\mu_0 \frac{\partial H}{\partial t} \tag{2.10}$$

$$\nabla \times H = \frac{\partial D}{\partial t} \tag{2.11}$$

where the electric displacement vector is defined $D = \epsilon_0 E + P$ and the magnetic field strength H is related to the magnetic flux by $B = \mu_0 H$. Equations 2.10 and 2.11 are the Maxwell equations describing light propagation through a transparent, non-magnetic material, the usual current density J is absent as it is assumed that the material is transparent at the frequencies of the propagating waves.

Equation 2.11 can be expressed explicitly in terms of the driving field and the induced polarisation.

$$\nabla \times H = \frac{\partial}{\partial t} (\epsilon_0 E + P) \tag{2.12}$$

Taking the curl of Equation 2.10,

$$\nabla \times \nabla \times E = -\mu_0 \frac{\partial}{\partial t} (\nabla \times H) \tag{2.13}$$

Substituting from Equation 2.11, and noting the Maxwell divergence relation, $\nabla \cdot E = 0$ yields,

$$\nabla \times \nabla \times E = \nabla (\nabla \cdot E) - \nabla^2 E = -\mu_0 \frac{\partial^2}{\partial t^2} (\epsilon_0 E + P) \tag{2.14}$$

Rearranging Equation 2.14 gives the wave equation describing the electric field in the medium generated by the driving polarisation, and is general for all processes described in terms of polarisation. [26]

$$c^2 \nabla^2 E - \frac{\partial E^2}{\partial t^2} = \frac{1}{\epsilon_0} \frac{\partial P^2}{\partial t^2} \tag{2.15}$$

For second-order nonlinear interactions the general case may be described by the interaction of three photons, or Fourier components of a field. This analysis if thus limited to considering three frequencies ω_1, ω_2, and ω_3, defining the corresponding fields described by Equation 2.16. The system is generalised to one dimension, corresponding to light propagating along an arbitrary direction defined as z, such that $\frac{\partial}{\partial y}$ and $\frac{\partial}{\partial x}$ operating on the optical field are negligible. The form of the waves have been simplified to monochromatic, infinite plane waves

$$E_j (z,t) = \frac{1}{2} \left[A_j e^{-i(w_j t - k_j z)} + c.c \right], \qquad j \in \{1,2,3\} \tag{2.16}$$

In this description of the jth Fourier component of the $\boldsymbol{E}$ field, A_j is the slow time varying amplitude or envelope defined by $A_j = \sqrt{\frac{n_j}{\omega_j}} E_j$. In this derivation, it will be assumed that the depletion of energy from the pump wave of frequency ω_3 is negligible, and the amplitude in therefore a slowly varying term, A_j.

The polarisation field $\boldsymbol{P}$,defined by Equation 2.7, and the optical field $\boldsymbol{E}$ given by Equation 2.16 are substituted into the wave equation, Equation 2.15 and the required

differentiations are performed. The slowly-varying amplitude approximation implies that

$$k\frac{\partial A}{\partial z} \gg \frac{\partial^2 A}{\partial z^2}$$

$$\omega A \gg \frac{\partial A}{\partial t} \tag{2.17}$$

$$\omega^2 P \gg \omega\frac{\partial P}{\partial t} \gg \frac{\partial^2 P}{\partial t^2}$$

allowing several terms to be neglected. Subsequent rearrangement yields the coupled wave equations, written explicitly for $j = 1, 2, 3$ in the following equations [27]

$$\frac{dA_1(z)}{dz} = i\kappa_1 A_3(z) A_2^*(z) e^{i\Delta kz} \tag{2.18}$$

$$\frac{dA_2(z)}{dz} = i\kappa_2 A_3(z) A_1^*(z) e^{i\Delta kz} \tag{2.19}$$

$$\frac{dA_3(z)}{dz} = i\kappa_3 A_1(z) A_2(z) e^{-i\Delta kz} \tag{2.20}$$

where $\kappa_i = \omega_i d'/n_i c$. The nonlinear susceptibilities act as the coupling coefficients, and govern the transfer of energy between the different Fourier components of the field. The solution of Equations 2.18-2.20, the coupled wave equations for a particular case, is the basis for the analysis of specific nonlinear interactions as was first demonstrated by Armstrong et al [22]

2.3 Parametric Amplification

The coupled wave equations, equations 2.18-2.20 can be solved for the particular case of Optical Parametric Generation or Amplification. The assumption is made that the depletion of the pump field as it propagates through the nonlinear medium is negligible and hence $dA_3/dz = 0$. Noting that the signal and idler are interchangeable, the interaction can then be described by the solution of two coupled wave equations, specifically equations 2.21 and 2.22.

$$\frac{dA_1(z)}{dz} = i\kappa_1 A_3(z) A_2^*(z) e^{i\Delta kz} \tag{2.21}$$

$$\frac{dA_2(z)}{dz} = i\kappa_2 A_3(z) A_1^*(z) e^{i\Delta kz} \tag{2.22}$$

The general solution for these coupled equations assumes that both signal and idler fields are present in the initial condition, $A_1(0), A_2(0) \neq 0$. The coupled wave equations are readily solved [22, 21, 20, 26] yielding the solutions shown below in equations 2.23 and 2.24.

$$A_1(z) e^{-i(\Delta kz/2)} = A_1(0)\left[\cosh(gz) - \frac{i\Delta k}{2g}\sinh(gz)\right] + i\frac{\kappa_1}{g}A_2^*(0)\sinh(gz) \tag{2.23}$$

$$A_2(z) e^{-i(\Delta kz/2)} = A_2(0)\left[\cosh(gz) - \frac{i\Delta k}{2g}\sinh(gz)\right] + i\frac{\kappa_1}{g}A_1^*(0)\sinh(gz) \tag{2.24}$$

where the coupling parameter κ is described by

$$\kappa_j = \frac{\omega_j d'}{n_j c} A_3 \tag{2.25}$$

and

$$g = \sqrt{\kappa_1 \kappa_2 - \left(\frac{\Delta k}{2}\right)^2} \tag{2.26}$$

This general expression can be greatly simplified to describe a parametric amplifier. The assumption is made that only one input exists and that the system is phase matched, then it follows from the coupled equations 2.23 and 2.24 that

$$A_1(z) = A_1(0)\cosh(gz) \tag{2.27}$$

$$A_2^*(z) = i\frac{\kappa_2}{g} A_1^*(0)\sinh(gz) \tag{2.28}$$

The solutions expressed by Equations 2.27 and 2.28 indicate that power flows from the pump field to the signal and idler fields via the coupling parameter κ which is a function of the pump field amplitude. It can be shown that these equations along with the complete coupled wave equations 2.18-2.20, yield the result

$$-\frac{d}{dz}(A_3 A_3^*) = \frac{d}{dz}(A_1 A_1^*) = \frac{d}{dz}(A_2 A_2^*) \tag{2.29}$$

where the quantity $A_j A_j^*$ is proportional to the photon flux at a particular field component ω_j. This relationship therefore states that for each photon depleted from the pump field(ω_3), one photon is generated in both the signal(ω_1) and idler(ω_2) fields. Energy conservation allows an extension of equation 2.29 by means of integration over the entire interaction volume, resulting in the relationship shown in equation2.30

$$-\Delta\left(\frac{P_3}{\omega_3}\right) = \Delta\left(\frac{P_1}{\omega_1}\right) = \Delta\left(\frac{P_2}{\omega_2}\right) \tag{2.30}$$

where P_j denotes the beam power for the field component ω_j. Equation 2.30 relates the change in total power over an interaction and is known as the Manley-Rowe relation [21].

The parametric gain of the interaction with respect to the initial signal field is defined as

$$G(l) = \frac{I_1(z=l)}{I_1(z=0)} - 1 = \frac{|A_1(z=l)|^2}{|A_1(z=0)|^2} - 1 \tag{2.31}$$

where l is the interaction length and I is the intensity given by $I = nc\epsilon_0 EE^*/2$. The general solution to this problem is difficult. The following expression is the net fractional gain in signal intensity for a negligibly depleted, plane wave pump, with zero idler input and non-zero signal input, in a perfectly phase matched system.

$$G(l) = \cosh^2(gz) - 1 \tag{2.32}$$

For non-phase-matched systems, a simplified solution can be found again under the infinite plane wave, non-depleted pump approximation, with the additional constraint that the gain is low. The signal gain of a parametric amplifier is given by Equation 2.33 [27, 26].

$$G(l) = \Gamma^2 l^2 \frac{sin^2[\Gamma^2 l^2 - (\Delta k l/2)^2]^{1/2}}{[\Gamma^2 l^2 - (\Delta k l/2)^2]} \tag{2.33}$$

where Γ is the gain factor defined by

$$\Gamma^2 = \frac{8\pi^2 d_{eff}^2}{c\epsilon_0 n_1 n_2 n_3 \lambda_1 \lambda_2} I_3(0) \tag{2.34}$$

Equation 2.33 explicitly states the phase dependence of the signal gain, prompting a possible description of such a system as a phase dependent amplifier.

2.4 Phase Matching

The phase dependence of Equation 2.33 emphasizes the necessity for phase matching to provide high conversion efficiency for a nonlinear interaction. The net fractional signal gain for parametric generation, as described by Equation 2.33 includes a $sinc^2$ term which describes this phase dependence.

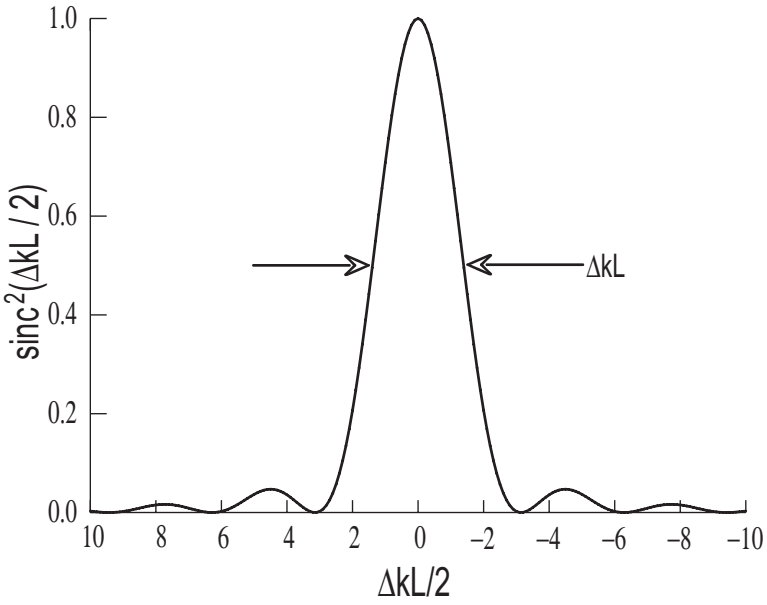

Figure 2.2: Plot of the $sinc^2$ phase matching function, showing the phase matching bandwidth ΔkL.

The function profile, Figure 2.2, clearly implies that even a small deviation from perfect phase matching will result in a dramatic reduction in the conversion efficiency of the interaction and hence the signal gain. Maximum gain occurs when the phase mismatch $\Delta k = 0$. The energy conservation equation and the phase matching condition, Equations 1.1 and 1.3 respectively, are not satisfied under normal circumstances. Under normal propagation conditions, the three field components do not maintain phase velocity synchronism due to material dispersion, resulting in a phase mismatch, and ultimately a periodic exchange of energy between the pump and generated fields. Several techniques have been developed such that the generated and pump fields propagate in phase.

2.4.1 Angle Phase Matching

For light propagating through normally dispersive materials, the ordinary index of refraction increases monotonically as a function of the optical frequency. Clearly it is this

characteristic which forbids perfect phase matching in such a situation.

Birefringent materials however, offer a means of achieving phase synchronism between different frequency components of the optical field. Such materials allow the propagation of two orthogonally polarised modes at a single frequency. The anisotropy of the crystal structure in such a material requires that these orthogonal modes experience different refractive indices. One of the modes, known as the ordinary mode, experiences a constant refractive index $n^o(\omega)$, with respect to the propagation direction. The orthogonal, extraordinary mode however, experiences a refractive index $n^e(\omega, \theta)$ which varies as a function of the propagation direction. The tensorial relationship between the optical field and the induced polarisation field allows coupling of waves between field components in different polarisation states. It is therefore possible in some circumstances, to find an angle of propagation (with reference to the principle optical axis) such that the phase velocities of the pump and generated waves are equal. This technique is known as Angle Phase Matching and the phase matching angle is denoted by θ_{pm}.

2.4.2 Quasi-Phase Matching

Angle phase matching requires the angle tuning of a birefringent crystal in order to nullify the group velocity mismatch between different frequency components of the optical field. This method however, has some disadvantages arising from the dependence on the propagation angle and the requirement for specific crystal symmetry groups which allow optical birefringence. The phase matching angle θ_{pm} is not in general, that which describes the propagation direction allowing the largest d_{eff} and hence the strongest nonlinear response. Furthermore, crystals with cubic symmetry are optically isotropic and hence birefringence cannot be used to angle phase match a nonlinear interaction in such a medium. This is of relevance as the diagonal element of the nonlinear susceptibility tensor for a crystal with cubic symmetry is large and allows a strong nonlinear interaction. It would be desirable for a phase matching technique to allow propagation along a direction corresponding to one of these diagonal terms.

In the case where a phase velocity mismatch exists between the pump wave and the generated wave, the relative phase difference between the generated wave and the driving polarisation will increase (from zero) to $\pi/2$ after propagating a distance through the nonlinear medium, defined as the coherence length of the interaction. The coherence length L_c can be defined as the distance over which the $sinc^2(\Delta k/2)$ phase dependence term of the small signal gain goes to zero as in Equation 2.35.

$$L_c = \frac{\pi}{\Delta k} \tag{2.35}$$

In the first coherence length, energy flows from the pump field into the lower frequency, generated signal field. As the waves travel a distance beyond the first coherence length, energy begins to flow back from the signal field to the pump, clearly an undesirable situation in terms of conversion efficiency of the nonlinear interaction. A phase correction of π radians after each subsequent coherence length traveled by the waves in the medium allows a continual flow of energy from the pump to the signal and hence the monotonic growth of the signal field. In such a case however, the growth of the signal field is not as rapid as would be experienced in a perfectly phase matched system, leading to the description of this technique by the term Quasi-Phase Matching (QPM) [24].

Armstrong et.al [22] were the first to propose experimental means of achieving Quasi-Phase Matching. Inverting the sign of the nonlinear susceptibility tensor after each coher-

ence length achieves the required π phase correction. The most conceptually simple model requires that the nonlinear crystal is segmented into sections one coherence length thick, and that each section is oriented such that the nonlinear polarisation is shifted by π radians, as in Figure 2.3. This can be achieved in a non-centrosymmetric crystal by a rotation of the crystal by 180^o about the propagation axis, due to the lack of inversion symmetry. The periodic reversal of the ferroelectric domain polarity and hence modulation of the nonlinear susceptibility lead this technique to be referred to as periodic poling.

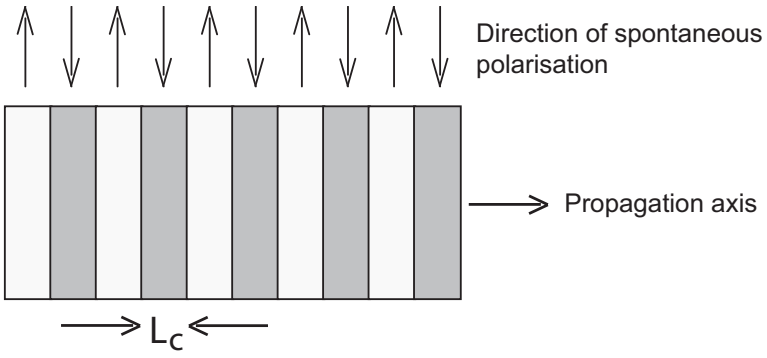

Figure 2.3: Schematic of the *stack-of-plates* quasi-phase matching method.

This model was first analysed by McMullen, referring to the technique as the stack-of-plates method [28]. The analysis considers a stack of n identical plates of thickness equal to one coherence length, oriented such that the nonlinear polarisation in every other plate is phase shifted by π radians. The problem is generalised for an arbitrary nonlinear interaction by considering three forward-traveling collinear beams propagating through the stack. The more intense beam acts as the pump wave and the non-depleted pump approximation is made. Furthermore, it is not a requirement that subsequent plates are in contact, it is assumed however, that the relative phase does not slip between the output and input of adjacent plates. The effective nonlinear coefficient of the nth slab is then described by Equation 2.36.

$$d_{eff}(n) = (-1)^{n-1} d_{eff} \tag{2.36}$$

The coupled wave equations are then solved for a particular nonlinear interaction. Equation 2.37 shows the second harmonic generation (SHG) conversion efficiency for the infinite plane wave, non-depleted pump approximation for mth order Quasi-Phase Matching. The order of the Quasi-Phase Matching refers to the number m, of coherence lengths defining the thickness of each slab. The model described above is clearly first order ($m = 1$) QPM. For comparison, the corresponding equation for the case of Angle Phase Matching is shown in Equation 2.38.

$$\eta_{2\omega_{(QPM)}} = \frac{8\pi^2 d_{eff}^2 I_\omega}{\epsilon_0 n_\omega^2 n_{2\omega} c \lambda_\omega^2} (NL_c)^2 (2/m\pi)^2 \tag{2.37}$$

$$\eta_{2\omega_{(\theta_{pm})}} = \frac{8\pi^2 d_{eff}^2 I_\omega}{\epsilon_0 n_\omega^2 n_{2\omega} c \lambda_\omega^2} L^2 \tag{2.38}$$

Quasi-Phase Matching is used as a technique to tune the output of a nonlinear interaction. The fact that the energy conservation condition does not predict a unique solution, that is, a unique pair of signal and idler photons, allows the frequency of the

signal and idler photons to be tuned by altering the phase matching parameters. In Angle Phase Matching, the propagation direction is the main tuning parameter. In the case of Quasi-Phase Matching, the poling (or grating) period is the parameter of interest.

The phase velocity synchronism (or momentum conservation) equation in the presence of a grating such as a periodically poled crystal is given in Equation 2.39.

$$\Delta k = k_p - k_s - k_i - k_g \tag{2.39}$$

where k_p, k_s and k_i refer to the wave vector of pump, signal and idler respectively, and k_g is the grating vector defined by $k_g = 2\pi/\Lambda_g$ where Λ_g is the grating period. In a perfectly phase matched system the phase velocity mismatch $\Delta k = 0$, thus the quasi-phase matching condition is described by Equation 2.40.

$$\frac{n_p}{\lambda_p} - \frac{n_s}{\lambda_s} - \frac{n_i}{\lambda_i} - \frac{m}{\Lambda_g} = 0 \tag{2.40}$$

Coarse tuning is commonly achieved by manufacturing crystals with a number of different grating periods, such that a linear translation of the crystal will allow propagation through a different grating region and hence change the signal and idler frequencies. Clearly, fine tuning of the output frequencies can be achieved by any method which produces a small change in the grating period. Angle tuning is one such technique which allows tuning, though only over a small range which is limited by the small physical dimensions of the crystal [29]. The most common fine tuning technique is temperature tuning which alters the refractive indices of the material and also causes a change in the physical dimension of the grating due to thermal expansion. Combined, these effects change the phase matching parameters and hence allow a fine tuning of the signal and idler frequencies. Hence, continuous tuning over a broad spectral range of the output frequencies of a nonlinear interaction can be achieved by temperature controlling a multi-grating crystal.

Chapter 3: Optical Parametric Oscillator

The multitude of scientific applications requiring laser light of a specific wavelength exceeds the finite number of lasing media and their limited spectral range. Nonlinear optical interactions provide a mechanism for conversion from the already-available output frequency of lasers to frequencies fulfilling the requirements of a specific experiment or application. The simplest and earliest used techniques such as Second Harmonic Generation and Sum and Difference Frequency Generation result in output at new frequencies, but always in a unique relationship to the original frequency of one or more lasers. The optical parametric process however, is not restricted to a unique pair of output frequencies for the same input conditions. A continuous set of non-unique solutions is available and hence a continuous range of output frequencies can be generated from a single pump frequency. This characteristic has provoked great interest and wide application of optical parametric devices for providing tunable coherent radiation. The design of an optical parametric device to generate a tunable infrared source was pursued in this project.

3.1 Spontaneous Parametric Fluorescence

Spontaneous Parametric Fluorescence, often thought of as the inverse process of Sum Frequency Generation, describes the spontaneous break down of a photon into two lower frequency photons. This is different to Optical Parametric Amplification in the fact that there is only a single pump beam present in the input. Parametric fluorescence is a quantum mechanical phenomenon, however semiclassical theoretical models can be used to adequately describe the effect.

Consider a pump photon of frequency ω_p propagating in a nonlinear medium. The pump photon may spontaneously break down into a signal and idler photon of lower frequency ω_s and ω_i as seen in Figure 3.1. No real material excitation is involved, rather the material acts as a catalyst, generating photons at new frequencies through the nonlinear polarisation [24]. Energy conservation demands the sum of the generated frequencies equals the pump frequency, $\omega_s + \omega_i = \omega_p$. As discussed above however, the frequency condition imposed on the process due to the energy conservation requirement does not predict a unique solution. This is in contrast to the inverse process, Sum Frequency Generation, which clearly demands a single solution. This subtle difference is of great consequence and is the source of the immense utility of optical parametric processes.

The quantum mechanical nature of Spontaneous Parametric Fluorescence is evident in the fact that the signal and idler frequencies have zero input intensity. Classically, a

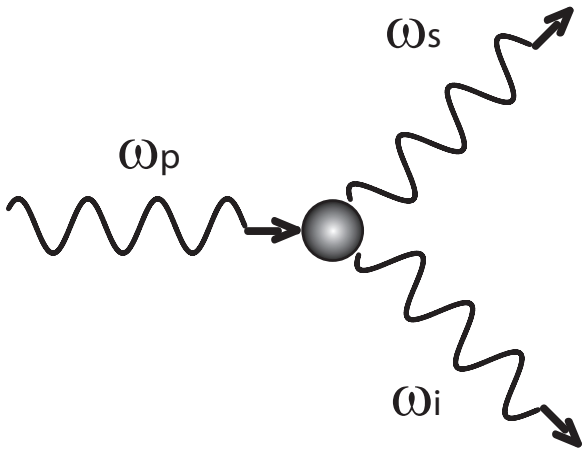

Figure 3.1: Spontaneous Parametric Fluorescence process. The pump photon with energy $\hbar\omega_p$ spontaneously splits into the signal and idler photons with energies $\hbar\omega_s$ and $\hbar\omega_i$ respectively.

field containing no photons cannot be amplified to some nonzero output term. Quantum mechanically however, this can be thought of as an amplification of the zero point fluctuations or vacuum noise at particular phase-matched frequencies [21].

3.2 Parametric Amplification

Optical Parametric Amplification is a three wave mixing process, which describes the flow of energy from a pump field to two lower frequency output fields, namely the signal and idler fields, satisfying the energy conservation relationship $\omega_s + \omega_i = \omega_p$. As a mixing process, some input at the generated frequencies ω_s or ω_i is required. This can be achieved by seeding the interaction with a beam at either of these frequencies, or more commonly by relying on the spontaneous breakdown of pump photons into photons at these frequencies through the Spontaneous Parametric Fluorescence mechanism described above. In this circumstance, the process can be described as the mixing of the zero-point flux of the signal and idler fields with the pump field through the nonlinear polarisation [27, 21, 30].

Spontaneous Parametric Fluorescence requires only the conservation of energy and hence does not predict a unique pair of signal and idler photons as the output of the interaction. The Parametric Amplification process however, does ideally provide an output field with intensity at a single pair of frequencies (a real interaction will result in some finite bandwidth about these frequencies). This occurs as a result of phase matching.

As with all nonlinear interactions, phase velocity synchronism must occur in order to achieve high conversion efficiency from the pump to the generated frequencies. This requirement is equivalent to conservation of linear momentum. The simultaneous conservation of energy and momentum is not satisfied in general, and is the subject of phase matching issues as discussed in Section 2.4. Tuning the phase matching parameters of nonlinear interactions with non-unique solutions, such as optical parametric amplification, provides continuous frequency tunability of the pairs of generated photons which satisfy the phase matching condition.

The following subsections will discuss the parametric gain for the parametric amplification process in situations where various approximations hold. The notation and results follow those detailed by Sutherland [24]. It is assumed that the interaction takes place in

a single pass of a nonlinear optical crystal, under which conditions the gain is modest and hence it is assumed that pump depletion is negligible. In each case, the parametric gain G is defined as expected through Equation 3.1.

$$\frac{P_p(L)}{P_p(0)} = 1 + G \tag{3.1}$$

where $P_p(z)$ denotes the pump power after propagating a distance z through the nonlinear medium.

The general form of the parametric gain G for small gain is as in Equation 3.2

$$G \approx (gL)^2 \frac{sin^2(\Delta kL/2)}{(\Delta kL/2)^2} \tag{3.2}$$

which simplifies to $G \approx (gL)^2$ for perfect phase matching, where g is known as the gain coefficient.

Furthermore, in each case, the gain coefficient includes a term known as the degeneracy factor δ which is defined by Equations 3.3 and 3.4.

$$\omega_s = \frac{1}{2}\omega_p(1+\delta) \tag{3.3}$$

$$\omega_i = \frac{1}{2}\omega_p(1-\delta) \tag{3.4}$$

where $\delta \in [0, 1]$. The degenerate point where $\omega_s = \omega_i = \frac{1}{2}\omega_p$ corresponds to $\delta = 0$ and describes the inverse interaction of second harmonic generation. The gain coefficient is maximised at this point and thus the degenerate wavelength $\lambda_0 = 2\lambda_p$ and the refractive index at the degenerate wavelength $n_0 = n(\lambda_0)$ are defined as references.

3.2.1 Infinite Plane Wave

An Infinite Plane Wave can be used to describe the interacting fields when the beam sizes are large with respect to the crystal length and aperture length of the crystal. The gain coefficient is given by Equation 3.5 [24]

$$(gL)^2 = \frac{16\pi^2 d_{eff}^2 L^2}{\epsilon_0 n_0^2 c \lambda_0^2} P_p(1-\delta^2)\frac{1}{2n_p A} \tag{3.5}$$

where A is the cross sectional beam area. An equivalent expression for the gain for this model of parametric amplification is derived in Section 2.3. The gain factor $\Gamma = (gL)^2$. This can easily be verified assuming $n_0 \approx n_s \approx n_i$ and explicitly converting from intensity(flux density) to power(flux).

3.2.2 Focused Gaussian Beam

Focusing the beams and hence decreasing their cross sectional area results in an increase in the parametric gain, as is evident in the A^{-1} dependence of Equation 3.5. Focusing the beams results in a deviation from the infinite plane wave model. To adequately describe the situation of focused beams, a Gaussian radial dependence of the beams is assumed. This model is valid in the case where the crystal length is less than the order of the confocal parameters of the interacting beams [27, 31]. It is assumed that the signal and

idler share a common confocal parameter. The confocal parameter b is defined in terms of the Rayleigh range z_R by Equation 3.6 [24]

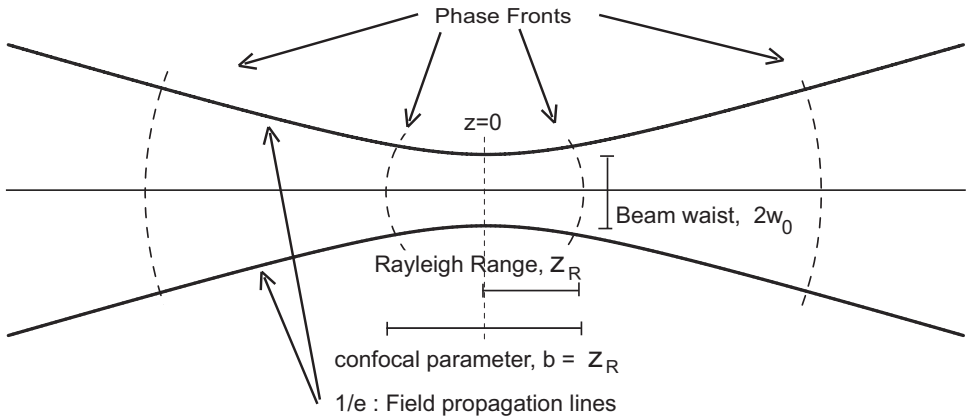

Figure 3.2: Beam propagation profile of a TEM_{00} Gaussian beam, showing the confocal parameter b

$$b = 2z_R = \frac{2n\pi w_0^2}{\lambda} \tag{3.6}$$

where the beam waist $2w_0$ is the minimum $1/e$ width of the Gaussian beam profile as seen in Figure 3.2. The Rayleigh range is the distance from the focal plane at which the beam radius is a factor of $\sqrt{2}$ greater than it is at the waist.

Interacting beams with Gaussian radial dependence do not in general optimally overlap, causing a reduction in the parametric gain with respect to that predicted using the plane wave model. The near field gain reduction parameter K^2 which accounts for this is a function of the pump, signal and idler beam radii and is defined in Equation 3.7.

$$K = \frac{w_s w_i w_p}{w_s^2 w_i^2 + w_s^2 w_p^2 + w_i^2 w_p^2} \tag{3.7}$$

where w_j is the $\frac{1}{e^2}$ radius of the jth beam.

The gain coefficient in the near-field focused Gaussian beam model is given by Equation 3.8.

$$(gL)^2 = \frac{16\pi^2 d_{eff}^2 L^2}{\epsilon_0 n_0^2 c \lambda_0^2} P_p (1-\delta^2) \frac{4K^2}{n_p} \tag{3.8}$$

The gain coefficient is heavily dependent on the near field gain reduction parameter. Optimising this parameter will result in a desirable increase in the parametric gain. Equating the partial derivative $\partial K/\partial w_p$ to zero yields the optimum condition on the pump beam radius (the physical parameter which can be most easily modified by optical

elements) which is given in Equation 3.9.

$$\frac{1}{w_p^2} = \frac{1}{w_s^2} + \frac{1}{w_i^2} \tag{3.9}$$

This condition combined with Equation 3.7 yields the maximum value of K^2 given in Equation 3.10.

$$K_{max}^2 = \frac{1}{4}(\frac{1}{w_s^2 + w_i^2}) \tag{3.10}$$

The intensity of the propagating beam will only be large within the confocal parameter (centered at the beam waist). It can be deduced from Equation 3.9 and an energy conservation equivalent condition $\frac{1}{\lambda_p} = \frac{1}{\lambda_s} + \frac{1}{\lambda_i}$ that if the signal and idler beams are confocally focused, then so is the pump beam. Equating the confocal parameters of the signal and idler beams $b = \frac{2\pi n w_0^2}{\lambda}$ to the maximum interaction length, the crystal length L, the following expression can be found for $G|_{M_{max}}$, the optimized near field confocal gain.

$$(gL)^2 = \frac{16\pi^2 d_{eff}^2 L^2}{\epsilon_0 n_0^2 c \lambda_0^2} P_p (1 - \delta^2) \frac{1}{\lambda_0 L} \tag{3.11}$$

In this optimized case the gain is proportional to L, not to L^2 as it is in the general near-field case.

3.2.3 Arbitrarily Focused Gaussian Beam

The effects of arbitrarily tightly focused beams will now be considered. The first analysis of Boyd and Klienman [32] assumes that the pump and signal beam share a common confocal parameter. The later analysis of Guha et. al [33] does not rely on this assumption and gives a more general result. These two cases will be dealt with separately in the following sections.

Common Confocal Parameter

The focusing of a Gaussian beam can be described in terms of a focusing parameter ξ defined by Equation 3.12.

$$\xi = L/b \tag{3.12}$$

The treatment of Boyd and Klienman [32] provides an expression which is valid for arbitrary values of ξ. The analysis is valid in the regime where the interaction length is greater than or similar to the confocal parameter of the beam. It is also assumed that the pump, signal and idler beam have a common confocal parameter. This requires that they also have equal focusing parameters, that is $\xi_p = \xi_s = \xi_i$.

An extraordinary wave propagating through a birefringent medium will not in general have a wave vector which is parallel to the Poynting vector. This directional difference between the extraordinary wave propagation direction and the direction of energy propagation results in the extraordinary beam appearing to 'walk off' the axis of the ordinary beam. This effect is due to crystal double refraction and is commonly known as the walk-off effect.

The energy of the generated wave experiences a walk-off of a finite angle ρ from that of the incident pump wave, limiting the effective volume over which mixing processes and

hence Parametric Amplification can occur efficiently [34]. This is due to the fact that non-collinearly propagating beams of finite size cannot optimally overlap over the entire length of the nonlinear medium.

An observation of the equations describing parametric gain shows that focusing the pump beam and hence reducing it's size will enhance the gain of the interaction (this is most clearly seen in Equation 3.5). The discussion above regarding walk-off however, suggests that beam focusing comes at an expense, specifically the reduction in the interaction volume over which parametric amplification is efficient. The walk-off effect in quantified in the theoretical analysis by the double refraction parameter B defined in Equation 3.13.

$$B = \rho\frac{\sqrt{k_\omega b}}{2} \tag{3.13}$$

Kleinman [35] described the reduction in gain due to walk-off by a characteristic length, known as the aperture length $L_a = \sqrt{\pi}w_0/\rho$. The aperture length is defined as the crystal thickness over which a generated beam incident at the crystal surface ($L = 0$), would just separate from the pump beam with the same aperture.

Boyd and Kleinman [32] evaluate nonlinear interactions with a gain reduction factor $\overline{h}$ which is a function of three parameters. These are the double refraction parameter B, the focusing parameter ξ and a phase matching parameter σ. The phase matching parameter σ is dependent on b and can be maximized experimentally through the tuning techniques (crystal orientation and temperature) discussed in Section 2.4. Thus, the gain reduction factor h_m for the optimum phase matching condition, corresponding to σ_m, can be defined by the focusing and double refraction parameters as in Equation 3.14.

$$\overline{h}_m(B,\xi) = max\left[\overline{h}(\sigma,B,\xi)\right]_\sigma \tag{3.14}$$

The optimised gain reduction factor h_m must be found numerically by solving the wave equation as the beams propagate through infinitesimal slabs of the nonlinear medium. Integration over all such slabs provides a complete model of the source, and hence the field amplitude outside the material. The power in the generated beam and hence the parametric gain is then found by integrating over the beam area in the far field. This is a somewhat complex procedure, recognized by the work of Chen and Chen [36], who developed a simple analytical function to obtain the results predicted by Boyd and Kleinman, in a more straightforward manner. The focusing dependence of the parametric gain can be observed by plotting the analytical functions derived by Chen and Chen, for the optimised gain reduction parameter $\overline{h}_m(B,\xi)$ as a function of the focusing parameter ξ as seen in Figure 3.3. It is noted that in the absence of the walk-off effect, the function behaves asymptotically, converging toward $\overline{h}_m(0,\xi) \rightarrow \xi$, as ξ goes to zero. This describes the parametric gain as the model tends toward the plane wave approximation [36].

The parametric gain for the optimized common confocal, tightly focused Gaussian beam model is given in terms of the usual parameters plus the additional focusing and double refraction parameters through the gain reduction factor $\overline{h}_m$ as in Equation 3.15.

$$(gL)^2 = \frac{16\pi^2 d_{eff}^2 L^2}{\epsilon_0 n_0^2 c\lambda_0^2} P_p(1-\delta^2)\frac{h_m(B,\xi)}{\lambda_0 L} \tag{3.15}$$

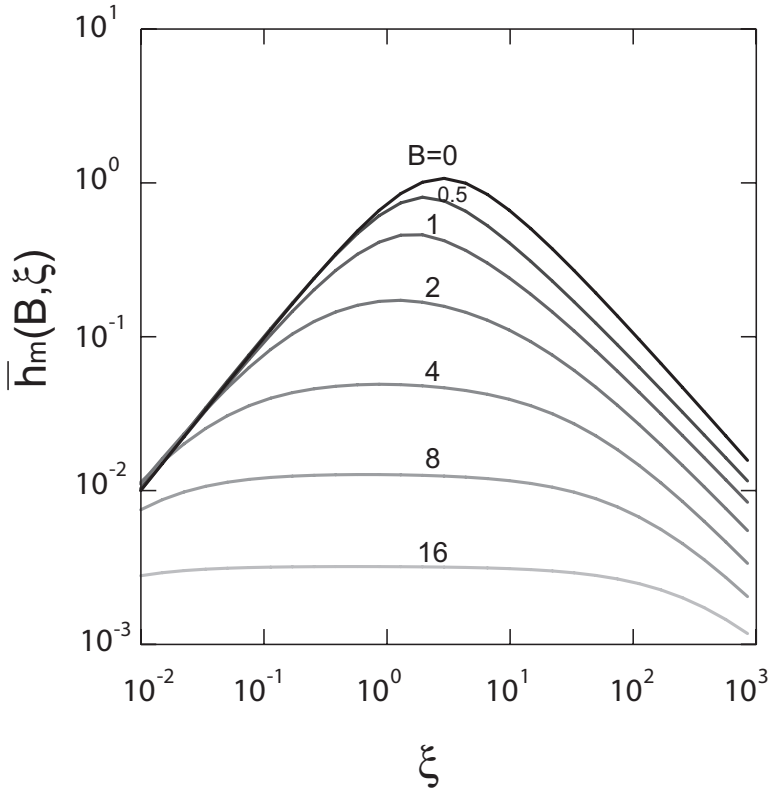

Figure 3.3: The gain reduction factor $\overline{h}_m$ as a function of the common focusing parameter $\xi \equiv \xi_s = \xi_p$ and various values of the walk-off parameter B.

Independent confocal parameters

The original analysis of Guha et al. [33] makes no a priori assumption as to the relative beam sizes as is the case with the model of Boyd and Klienman [32] which assumes that the generated signal (and idler) beams have the same confocal parameter as the pump beam. They assume that the beam sizes of the signal (and idler) are purely determined by the resonant optical cavity in the case of singly (and doubly) resonant Optical Parametric Oscillators. This treatment was updated by Guha [37] extending the analysis to include models for the near-threshold region and to include linear absorption at all three frequencies. Equation 3.16 gives the result derived in the earlier, simpler paper [33].

$$G = \frac{32\pi^2 d_{eff}^2 L}{\epsilon_0 n_s n_i \lambda_p \lambda_s \lambda_i} P_p \frac{h_{sm}(k, \xi_p, \xi_s)}{1+k} \tag{3.16}$$

where k is the ratio of the pump and signal wave vectors, that is $k = \frac{k_p}{k_s}$ and $h_s m$ is the function h_s maximized with respect to the phase mismatch $\Delta k L$.

3.3 Optical Parametric Oscillators

Most parametric interactions (limited by currently available nonlinear materials and pump lasers) operate in the low to moderate gain regime, with gains of only a few orders of magnitude. Macroscopic amplification of parametric waves from quantum noise in a single pass configuration, as is the case with unseeded parametric amplification, is not possible

at such low gain levels [27]. The required increase in net gain to make this possible can be achieved by providing positive feedback at the generated frequencies. Enclosing the nonlinear gain medium in a resonant optical cavity, allows amplification of parametric waves to macroscopic levels by successive passes through the nonlinear medium. At pump powers exceeding some threshold pumping power, the parametric gain of the resonator is sufficiently large to overcome the losses in the cavity, oscillation occurs, allowing the extraction of coherent output at the generated frequencies. Such a device is known as an Optical Parametric Oscillator.

Optical Parametric Oscillators have become widespread since the first demonstration of coherent, tunable, optical parametric oscillation by Giordmaine and Miller [38]. OPOs have now been developed, covering spectral ranges from the visible [39, 40] to the near- and far-infrared [41, 42, 43, 44].

Optical Parametric Oscillators are separated into two main categories. Those oscillators with cavities permitting the resonance of both generated frequencies (signal and idler) are known as Doubly Resonant Oscillators (DROs). Optical cavities which only permit resonance at one of the generated frequencies (typically the signal), are known as Singly Resonant Oscillators (SROs). Resonating only a single generated field in a SRO greatly relaxes the tolerances on the pump laser and OPO cavity [45]. This results in an increase in the threshold condition of one or more orders of magnitude. DROs however, encounter problems in regard to stability and smooth tuning [27]

In an SRO, only one generated field is resonant, so the generated wavelength is free to change continuously in order to preserve the conservation of energy requirement. This is necessary to accommodate fluctuations in the cavity resonant modes and thus allow stable operation [24]. DROs are much more susceptible to instability, as the resonant condition for both generated fields must be met simultaneously.

3.4 Singly Resonant Parametric Oscillators

In a Singly Resonant Optical Parametric Oscillator, the cavity mirrors are highly reflecting for only one of the generated waves, most commonly the signal. The first experimental report of an SROPO was by Bjorkholm [46], and in a subsequent paper [47] the superior stability of SROs as opposed to DROs was demonstrated. This effect is explained in terms of the axial mode spacings of the two different fields. The signal and idler modes in general, have unequal axial mode spacings and hence simultaneous resonance can only be achieved on certain axial modes which are clustered in groups, separated by a spacing period which is large compared with the axial mode spacing. This cluster effect gives rise to the tuning discontinuities and instability with respect to fluctuations in the oscillator parameters, which are observed in DROs. SROs do not experience the cluster effect and the various problems associated with it. Continuous tunability and stability are an issue in the design of an OPO as a light source for resonant infrared pulsed laser deposition, and hence the current project will involve the design of an SRO for this particular application. The following subsections will examine the theory of SROs, specifically that regarding the threshold power and conversion efficiency. The theory of DROs will be omitted.

3.4.1 Threshold

Oscillation can only occur in a resonant cavity, such as that forming an OPO, when the round-trip gain is greater than the round-trip cavity loss. Clearly then for an OPO, a

threshold condition exists on the parametric gain. Since the parametric gain is a function of the pump power (see Section 3.2), this threshold condition is commonly quoted in terms of a threshold pump power P_{th}, required to initiate parametric oscillation. In the case of the SRO, only the signal (or idler) is resonant, so that it is only the losses at the signal (or idler) frequency which are of concern.

Losses occur on reflection from all (non-ideal) mirrors, and attenuation due to the air path taken by the beam in the cavity. In this treatment, the distributed loss of the cavity at the signal frequency α_s will be defined in terms of the reflectivity of a single imperfect mirror, simplifying the analysis. This parameter R_s is defined as the round trip reflectivity of the cavity and is defined in Equation 3.17 [21].

$$\alpha_s L = 1 - R_s \tag{3.17}$$

An analysis of steady-state oscillation must require that the resonant field be reproduced at some arbitrary plane within the cavity, after each successive round trip of the cavity. Specifically, the parameters which must be reproduced are the shape, amplitude and phase of the propagating Gaussian beam. Such a requirement can be imposed via the ABCD law as described in the seminal paper on resonator theory by Kogelnik and Li [48], which uses a ray transfer matrix acting on the beam parameters to fully describe the propagation of Gaussian beams. The solution of the general oscillation condition, and hence the threshold gain condition for a SRO derived from this treatment is presented by Yariv [21] and is quoted in Equation 3.18.

$$(g_t L)^2_{SRO} = 2(1 - R_s) \tag{3.18}$$

where g_t is the threshold gain coefficient. For a SRO where the idler is resonant, Equation 3.18 holds upon substitution of R_i for R_s, where R_i is the round trip reflectivity of the idler for the cavity.

The statement made earlier in this section regarding the relative thresholds for DROs and SROs can be validated by comparing g_{tSRO} and g_{tDRO}. The doubly resonant threshold gain coefficient is given by $(g_{tDRO}L)^2 = (1 - R_s)(1 - R_i)$, the relative increase in the threshold gain for an SRO for the same value of R_s is given by Equation 3.19 [21].

$$\frac{(g_t L)^2_{SRO}}{(g_t L)^2_{DRO}} = \frac{2}{(1 - R_i)} \tag{3.19}$$

The threshold pump power for a SRO can easily be found by equating the threshold parametric gain condition of Equation 3.18 with the pump power dependent functions describing the parametric gain for the various models outlined in Section 3.2.

The equations describing the steady-sate threshold pump power for SROPOs under the various cases appear below.

Infinite Plane Wave

$$(P_p)_{th} = \frac{\epsilon_0 n_s^2 n_p c \lambda_p^2}{\pi^2 d_{eff}^2 L^2 (1 - \delta^2)} (1 - R_s) A \tag{3.20}$$

Focused Guassian Beams

$$(P_p)_{th} = \frac{\epsilon_0 n_s^2 n_p c \lambda_p^2}{8\pi^2 d_{eff}^2 L^2 (1-\delta^2) K^2}(1-R_s) \tag{3.21}$$

Optimized confocal near-field Focused Guassian Beams

$$(P_p)_{th} = \frac{\epsilon_0 n_s^2 c \lambda_p^3}{\pi^2 d_{eff}^2 L (1-\delta^2)}(1-R_s) \tag{3.22}$$

Optimized common-confocal parameter, tightly Focused Guassian Beams

$$(P_p)_{th} = \frac{\epsilon_0 n_s^2 c \lambda_p^3}{\pi^2 d_{eff}^2 L (1-\delta^2) h_m(B,\xi)}(1-R_s) \tag{3.23}$$

3.4.2 Conversion Efficiency

The efficiency of the conversion of energy from the pump field to the generated fields in an OPO is of interest. The conversion efficiency η can be defined by Equation 3.24.

$$\eta = \frac{P_s + P_i}{P_{p_i} n} \tag{3.24}$$

Kreuzer [49] carried out an analysis of the conversion efficiency of an SRO for the uniform plane wave model. The resulting expression is given in Equation 3.25.

$$\eta = \sin^2 \Gamma \tag{3.25}$$

where

$$\frac{\sin^2 \Gamma(x)}{\Gamma(x)} = \frac{1}{N_{SRO}} \tag{3.26}$$

The parameter N_{SRO} is defined as $N_{SRO} = \frac{(P_p)_{in}}{(P_p)_{th}}$, the number of times by which the input pump power exceeds the SRO threshold pump power [24].

This model predicts that 100 % conversion efficiency is achievable when the pump power is $N_{SRO} = (\pi/2)^2$ times above threshold.

Bjorkholm [50] derived the expression for the conversion efficiency of an SRO for Guassian beams. The resulting expression is given in Equation 3.27.

$$\eta = 1 - \left[\frac{1}{N_{SRO}} + \int_0^{\ln(N_{SRO})} e^{-x} \cos^2 \Gamma(x) dx\right] \tag{3.27}$$

where

$$\frac{\sin^2 \Gamma(x)}{\Gamma(x)} = \frac{e^x}{N_{SRO}} \tag{3.28}$$

The functions describing the conversion efficiency of a SRO in both the infinite plane wave and Gaussian beam models, are not simple analytical functions, and must be solved numerically. A function was written to perform the required numerical integration, and hence evaluate Equations 3.25 and 3.27, the result of which are shown in Figure 3.4.

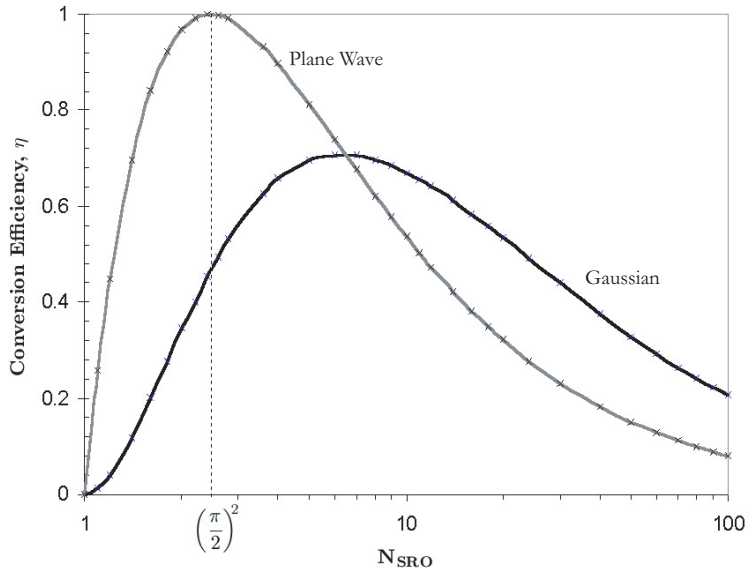

Figure 3.4: Conversion efficiency η as a function of the degree of pumping N_{SRO} for a Singly Resonant Oscillator. Uniform Plane Wave and Gaussian-beam solutions are shown for comparison.

It can be seen that the Gaussian beam model does not allow 100% conversion efficiency to be achieved. The maximum achievable efficiency using a Guassian pump beam is $\approx 71\%$ in this model, which occurs for $N_{SRO} \approx 6.5$ [50].

3.5 Pulsed Optical Parametric Oscillators

Whilst the SRO is an attractive configuration for an OPO, in terms of stability and simple tuning behavior, it has the highest threshold of all cavity configurations [27]. Overcoming this threshold is a major challenge when using conventional external pumping schemes and commonly available CW pump lasers. Given the further restrictions imposed by the nonlinear medium, the development of SROs was initiated with high-peak-power pulsed pump sources. The first demonstration of an OPO by Giordmaine and Miller [38] was in fact, a pulsed DROPO . The development of numerous SROPOs followed [47, 49, 51, 52]. All of these devices operated in the tens of nanoseconds pulse duration regime. In this regime, the resonator will in general (for cavities with length of the order $<$ 1m) allow multiple round trips of the signal (or idler) during a temporal period equal to the pulse duration and hence nanosecond OPOs can be treated similarly to CW OPOs. This cannot be the case for shorter pulses, as even in the tens of picoseconds pulse duration regime the cavity length must be on the order of a millimeter to permit a single round trip during the pulse duration time. Hence, picosecond and femtosecond OPOs must be treated separately from CW OPOs.

3.6 Synchronously Pumped Optical Parametric Oscillators

The high peak power available from mode-locked lasers allows sufficient nonlinear gain to overcome the required threshold for a singly resonant oscillator. Unlike nanosecond pulsed OPOs, picosecond or femtosecond pump pulses are too short to allow multiple round-trips,

and hence the build up of parametric waves within the pump pulse temporal duration.

Ensuring that the length of the OPO resonant cavity is such that the round-trip transit time for a single pulse is equal to the interpulse time of the pump laser, known as synchronous pumping, allows the threshold to be overcome. The resonated parametric pulse is amplified on successive transits of the cavity, drawing energy from consecutive coincidences with the incoming pump pulse [27]. Such a device is known as a Synchronously Pumped Optical Parametric Oscillator (SPOPO). The combination of the short pulse duration and high peak power from the mode-locked pump laser and the broad frequency tunability make SPOPOs a popular device in fields such as high-resolution time-domain spectroscopy [53, 54, 55] and are characteristics which are suitable for this project, an application in pulsed laser ablation.

Cheung and Liu [56, 57] present a comprehensive theory on the singly resonant, synchronously pumped OPO. The most important effects in this model are group velocity dispersion in the cavity; the group velocity mismatch causing a walk-off between the pump, signal and idler; the mismatch between the cavity length of the OPO and the pump laser; the pump depletion; and the parametric gain bandwidth. The SPOPO is modeled as a synchronously pumped laser, lasing at the pump frequency, with gain provided by the parametric amplification in the nonlinear medium. The model is developed to account for the effects listed above, evaluating the effects of the temporal and spatial mismatch of the pulses.

For ultrashort pulses, the spectral width of the interacting beams must be considered. The time-bandwidth product for a Gaussian beam is limited by the uncertainty principle, to a minimum value given in Equation 3.29. Hence for ultrashort pulses the spectral width is broad, a result which must be taken into account when considering phase matching.

$$\Delta\tau\Delta\nu \geq \frac{2\ln(2)}{\pi} \geq 0.44 \tag{3.29}$$

The phase matching condition is usually such that it is satisfied for the midband frequencies of the interacting waves. For ultrashort pulses this phase matching condition is not satisfied for all frequencies within the broad spectral width. The phase mismatch sets the gain bandwidth of the interaction, and hence in this case, the spectral width cannot be neglected when considering pump depletion near the phase-matched central frequencies. The phase matching bandwidth and hence the gain bandwidth of the nonlinear interaction $\Delta\omega$ is given in Equation 3.30.

$$\Delta\omega = \frac{2\pi c}{L}\left(n_i - n_s + \omega_i \frac{dn_i}{d\omega}|_{\omega_i} - \omega_s \frac{dn_s}{d\omega}|_{\omega_s}\right)^{-1} \tag{3.30}$$

The theory developed by Cheung and Liu [56] results in a nonlinear second-order differential equation describing the intra-cavity field envelope of the resonated signal pulse for the non-degenerate case. They present solutions obtained numerically using the finite difference method. The results of interest regard the effects of the effective detuning time and the peak pump intensity on the signal efficiency. The signal efficiency as a function of the normalized peak pump intensity is shown in Figure 3.5 [56].

McCarthy and Hanna [45] developed a simplified analytical model to describe a SPOPO to provide approximate quantitative guidelines for the design of such devices. It was derived with the purpose of clearly showing the effects on the threshold condition of parameters such as crystal length, group-velocity dispersion, walk-off and spectral

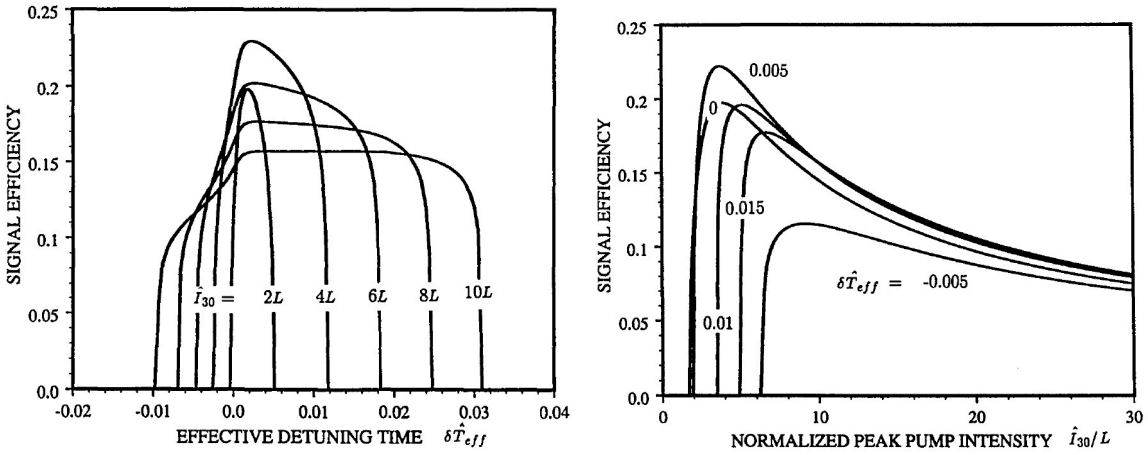

Figure 3.5: Output signal efficiency as a function of **(a)** the effective detuning time at various peak pump intensities. **(b)** the peak pump intensity at various normalized effective detuning times.

bandwidth. The effects of pump depletion are neglected as a simplification. The resulting expression for the pump threshold power accounts for the temporal overlap of pulses, with factors accommodating for both temporal walk-off and differences in peak shape (g_l and g_t respectively) as shown in Equation 3.31.

$$P_{p,th} = \frac{\epsilon_0 c n_s n_i n_p \lambda_s \lambda_i}{8\pi^2 d_{eff}^2 g_s g_t} \frac{L}{L_{eff}^2} \pi w_p^2 \tag{3.31}$$

where the correction factors g_s and g_t are defined in Equations 3.32 and 3.33 respectively.

$$g_t = \left(\frac{\tau_p^2}{\tau_p^2 + \tau_s^2} \right)^{1/2} \tag{3.32}$$

$$g_s = \frac{w_p^2}{w_s^2 + w_p^2} \tag{3.33}$$

where τ refers to the duration of Gaussian pulses and w_p and w_s are the radii of the pump and signal beams respectively. The effective interaction length is defined in Equation 3.34, where L_t is the temporal aperture length of the non linear interaction and erf is the error function.

$$L_{eff} = L_t \; erf \left(\frac{\sqrt{\pi}}{2} \frac{L}{L_t} \right) \tag{3.34}$$

For crystal lengths L that are large compared to the temporal aperture length L_t, the argument becomes large and the value of the error function goes to unity [45, 42]. This gives the expected result, that the effective interaction length L_{eff} is limited by the temporal aperture length L_t.

Chapter 4: Optical Parametric Oscillator Design

A broadly tunable, pulsed, coherent light source with high peak power is necessary for pulsed laser ablation of organic materials. These conditions have previously been met by Bubb et al. [5] using a Free Electron Laser at Vanderbilt University. The FEL produced picosecond pulses at gigahertz repetition rates with average powers of a few watts, continuously tunable from $2 - 10\mu m$. The aim of this project is to produce an alternative light source for polymer ablation, capable of producing comparable peak powers and tunable over an appropriate range. This was achieved through the design and construction of a synchronously pumped optical parametric oscillator.

The following chapter outlines the design of an SPOPO from which the idler frequency (at wavelengths centered around $3.4\mu m$) can be extracted.

4.1 Pump Laser

The properties of the pump laser are important considerations in the design of the SPOPO. The laser used to pump the OPO was a novel, mode-locked Nd:YVO_4 laser, designed and built at the Laser Physics Centre [58]. The laser oscillator is very long, allowing low repetition rates for the pulsed output. The particular configuration used in this experiment produced 13 picosecond pulses at a repetition rate of 28.4MHz.

The laser system consists of a master laser oscillator and a power amplification stage. The master oscillator consists of a Nd:YVO_4 crystal pumped by 18W of 805nm radiation provided by a laser diode. The output of the master oscillator, a few watts of 1064nm radiation, is then passed through the power amplifier stage. Here again, the gain material is a diode-pumped Nd:YVO_4 crystal. The beam makes multiple passes of the gain medium, such that the output is up to 50W average power of 1064nm radiation.

4.2 Nonlinear Material

The material requirements of the nonlinear material are outlined in this section.

In order to observe second-order nonlinear optical effects, d_{eff} must be on the order of $0.1pm/V$ or more. Various different nonlinear optical materials exist and are commercially available. Lithium Niobate ($LiNbO_3$) is such a material, which has been widely used as the gain medium in nonlinear optical devices. In fact, the first demonstration of an OPO by Giordmaine and Miller [38] was based on a $LiNbO_3$ crystal.

$LiNbO_3$ is not a naturally occurring crystal, but can be grown in relatively large crystals of high quality. The symmetry of the crystal structure results in $LiNbO_3$ being optically uniaxial. It is ferroelectric below a high Curie temperature ($T_c \sim 1150^oC$). Pure $LiNbO_3$ has a wide transparency window from the band-gap edge at $\sim 350nm$ to the first infrared vibrational absorption at $5\mu m$. This is a very favorable property, allowing interactions involving any frequencies in the visible and near- to mid-infrared spectral region. The extent of the transparency window into the infrared, is not apparent in all other commonly used nonlinear materials, and is one of the primary reasons for using $LiNbO_3$ for this application.

The use of quasi-phase matching allows access to the largest nonlinearities permitted by the crystal. Bulk periodically poled $LiNbO_3$ (PPLN) has been extensively used for quasi-phase matching nonlinear interactions since it was first demonstration by Myers et al. [59]. A Magnesium Oxide doped Periodically Poled Lithium Niobate (MgO:PPLN) crystal was chosen for the current project due to the favorable optical and physical properties it exhibits, outlined in the following section, and because of the commercial availability of high quality PPLN crystals.

Periodic poling of a ferroelectric material such as $LiNbO_3$ can be achieved by periodically reversing the ferroelectric domain polarity and hence inverting the nonlinear susceptibility tensor with a half period equal to the coherence length. The most successful technique for the manufacture of PPLN uses an applied external electric field to reverse ferroelectric domains. After this technique was first demonstrated by Yamada et al. [60], it has developed to allow the fabrication of fine and deep periodically inverted domain structures of precisely controlled period, defined by a lithographic mask. This technique allows excellent reproducibility, one of the attractive properties of PPLN [61].

Quasi-phase matching of $LiNbO_3$ allows access to the d_{33} component of the Kleinman d-tensor, corresponding to a propagation angle which is not phase matchable by birefringent angle tuning. In PPLN this yields a large effective nonlinearity of $d_{eff} = (2/\pi)d_{33}$ where $d_{33} = 27pm/V$ giving rise to high gain when used as the nonlinear gain material in an OPO [62]. Furthermore, periodically poled materials allow for non-critical phase matching without any walk-off effect thus enabling the use of longer crystals, giving access to a longer interaction length and hence greater conversion efficiency [62].

4.2.1 Photorefractive Damage

The photorefractive effect is a serious problem with $LiNbO_3$. The photorefractive effect (and the resulting photorefractive damage) refers to optically induced changes in the refractive index of a material due to an electric field dependent refractive index. This adversely affects the output beam quality and phase-matching stability. The photorefractive effect is facilitated by charge carrier migration and is therefore a large problem in ferroelectrics which exhibit a large photogalvanic response, such as $LiNbO_3$. The domain inversion in PPLN cancels the optically induced space-charge fields which cause the photorefractive effect, significantly reducing photorefractive damage with respect to bulk $LiNbO_3$ [63, 62].

Further reduction in photorefractive effects can be achieved by heating the material, or by doping the crystal with impurities, most commonly magnesium oxide [64]. Photorefractive damage remains in the crystal for some time after illumination, until the displaced carriers redistribute to give a homogeneous charge distribution. It is not however, permanent and can be erased by heating the crystal and facilitating the diffusion of carriers. Furthermore, heating the crystal whilst exposing it to the light source (such as when op-

erating an OPO) anneals the photorefractive damage in real time [65]. In practice this is achieved by housing the PPLN crystal in an oven operating at elevated temperatures (above $\sim 100^oC$). This is not an inconvenience, as the precise temperature control afforded by the crystal oven is a great aid in temperature tuning.

It has been found that doping PPLN with magnesium oxide (or other dopants such as Zn^{2+}, In^{3+} [66], Sc^{3+} [64] and Hf^{4+} [67]) significantly increases the photorefractive damage threshold [68, 64]. Periodically poled MgO doped lithium niobate (MgO:PPLN) is commonly used, and is commercially available for use in quasi-phase matched OPOs, and was used as the gain medium for the OPO designed for this project. The increase in the photorefractive damage power-density threshold is generally quoted to be at least four orders of magnitude, with reports of damage thresholds above $8MW/cm^2$ for 5.4% molMgO:$LiNbO_3$ as compared to $\sim 1kW/cm^2$ for undoped congruently grown $LiNbO_3$ at 532nm [69].

4.3 Quasi Phase Matching

The ability to fabricate periodically poled structures of precisely controlled period, renders the phase matching problem the subject of a straight-forward engineering design. The phase matching equation relating the grating period Λ_g to the optical properties of the material is given in Equation 4.1 [61].

$$\frac{\Delta k_Q}{2\pi} = \frac{n_p}{\lambda_p} - \frac{n_s}{\lambda_s} - \frac{n_i}{\lambda_i} - \frac{m}{\Lambda_g} = 0 \tag{4.1}$$

where m is the quasi-phase matching order and will be taken to be $m = 1$.

In order to calculate the required grating vector, an operating temperature must be chosen and the refractive indices of the proposed pump, signal and idler wavelengths must be known at that temperature.

4.3.1 Sellmeier Equations

The Sellmeier equation for a particular material is in general, an empirically derived wavelength-dependent function of the refractive index. More sophisticated (and useful) models take into account the temperature dependence of the refractive index by introducing temperature as a parameter of the modified Sellmeier equation. Jundt [70] presents the Sellmeier equation for the extraordinary index of refraction n_e of congruent lithium niobate. The Sellmeier equation is presented as in Equation 4.2.

$$n_e^2 = a_1 + b_1 f + \frac{a_2 + b_2 f}{\lambda^2 - (a_3 + b_3 f)^2} + \frac{a_4 + b_4 f}{\lambda^2 - a_5^2} - a_6 \lambda^2 \tag{4.2}$$

where the parameters a_j and b_j are the empirically derived Sellemeier coefficients given in Table 4.1 and f is the temperature parameter given in Equation 4.3.

$$\begin{aligned} f &= (T - T_0)(T + T_0 + 2 \times 273.16) \\ &= (T - 24.5^oC)(T + 570.82) \end{aligned} \tag{4.3}$$

where f is the temperature parameter at temperature $T(^oC)$, the offset nulls the parameter at 24.5^oC for simplicity of use at room temperature.

Coefficient	Value
a_1	5.35583
a_2	0.100473
a_3	0.20692
a_4	100
a_5	11.34927
a_6	1.5334×10^{-2}
b_1	4.629×10^{-7}
b_2	3.832×10^{-8}
b_3	-0.89×10^{-8}
b_4	2.657×10^{-5}

Table 4.1: Sellemeier Coefficients for congruently grown $LiNbO_3$

Jundt's model also accounts for thermal expansion of the crystal at elevated temperatures, by applying Equation 4.4.

$$L = L_{25^oC}[1 + \alpha(T - 25^oC) + \beta(T - 25^oC)^2] \tag{4.4}$$

where $\alpha = 1.54\times10^{-5}\ K^{-1}$ and $\beta = 5.3\times10^{-9}\ K^{-2}$ are the thermal expansion coefficients of $LiNbO_3$, describing the crystal length L, at temperature T with respect to the length of the crystal at room temperature L_{25^oC}.

It should be noted that the Sellmeier equations presented above were derived for congruently grown lithium niobate, and not for MgO:LiNb0$_3$. Sellmeier equations for 5mol% MgO:$LiNbO_3$ have been empirically derived by Zelmon et al. [71] based on measurements from 0.4 to 5.0μm. This is a significant, as previous Sellmeier equations for MgO:$LiNbO_3$ presented by Shen et al. [72] were derived from measurments in the range 0.54 to 1.34μm and hence were valid only over a limited spectral range, which doesn't include the proposed signal and idler wavelengths. Zelmon's Sellmeier equations for 5mol% MgO:$LiNbO_3$ however, are not temperature dependent, as were those of Jundt for congruent $LiNbO_3$.

The Sellmeier equation presented by Zelmon is of the form shown in Equation 4.5.

$$n_e^2 = 1 + \frac{A\lambda^2}{(\lambda^2 - B)} + \frac{C\lambda^2}{(\lambda^2 - D)} + \frac{E\lambda^2}{(\lambda^2 - F)} \tag{4.5}$$

where the Sellmeier coefficients are shown below in Table 4.2

Coefficient	Congruent $LiNbO_3$	5mol% MgO:$LiNbO_3$
A	2.9804	2.4272
B	0.02047	0.01478
C	0.5981	1.4617
D	0.0666	0.05612
E	8.9543	9.6536
F	416.08	371.213

Table 4.2: Sellemeier Coefficients for the extraordinary index of congruently grown $LiNbO_3$ and congruently grown $LiNbO_3$ doped with 5-mol.% MgO

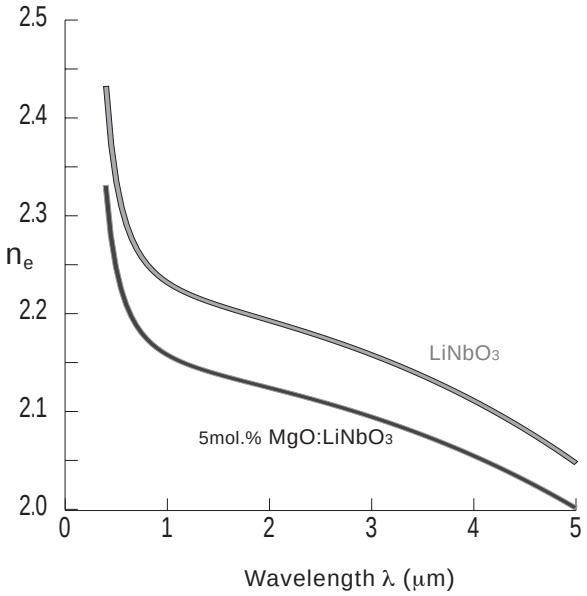

Figure 4.1: Sellmeier equations for 5mol.% MgO doped, and undoped congruently grown $LiNbO_3$ at 21^oC, defined by Equation 4.5.

The refractive index profiles of 5mol.% MgO doped, and undoped congruently grown $LiNbO_3$ at a temperature of 21^oC, as given by Zelmer's Sellmeier Equations (Equation 4.5 with coefficients from Table 4.2, are shown in Figure 4.1

4.3.2 QPM Grating Period Calculation

Using the Sellmeiers equation presented in the previous section, it is possible to calculate the grating period required to quasi-phase match a specific interaction, at a given operating temperature, in PPLN.

The interaction of interest here, is that which will produce idler radiation in the $3-4\mu m$ range, corresponding to a signal output in the $1450-1650nm$ range. A mean operating point must be chosen in order to perform the calculation, thus $3.4\mu m$ was chosen for the idler wavelength, corresponding to the resonant frequency of the C-H stretch mode in PEG (polyethylene glycol), a material successfully ablated using RIRPLD with a free-electron laser [5]. The pump, signal and idler wavelength are hence $\lambda_p = 1064nm$, $\lambda_s = 1550nm$ and $\lambda_i = 3.4\mu m$, such that energy conservation is satisfied.

The central operating temperature was chosen to be 150^oC, the elevated temperature selected to avoid possible photorefractive damage. The Sellmeier equation of Jundt, presented above in Equation 4.2, can then be used to predict the extraordinary refractive index of $LiNbO_3$. As no temperature dependent Sellmeier equations for MgO:$LiNbO_3$ exist in the literature, those for $LiNbO_3$ were used as the best available estimate.

The calculated values for the refractive index of $LiNbO_3$ for the pump, signal and idler, at a temperature of 150^oC, as predicted by the Sellmeier equations derived by Jundt are as follows, $n_p = 2.1619$, $n_s = 2.1435$ and $n_p = 2.0879$ as shown in Figure 4.2.

The grating period required to phase match this interaction can thus be calculated by solving Equation 4.1 for the grating period Λ_g (for first order QPM). The calculated grating period for the quoted values of λ_j and $n(\lambda_j)$, is $\Lambda_g = 29.56\mu m$. This gives the length of the grating period at the elevated temperature of 150^oC, which is larger than

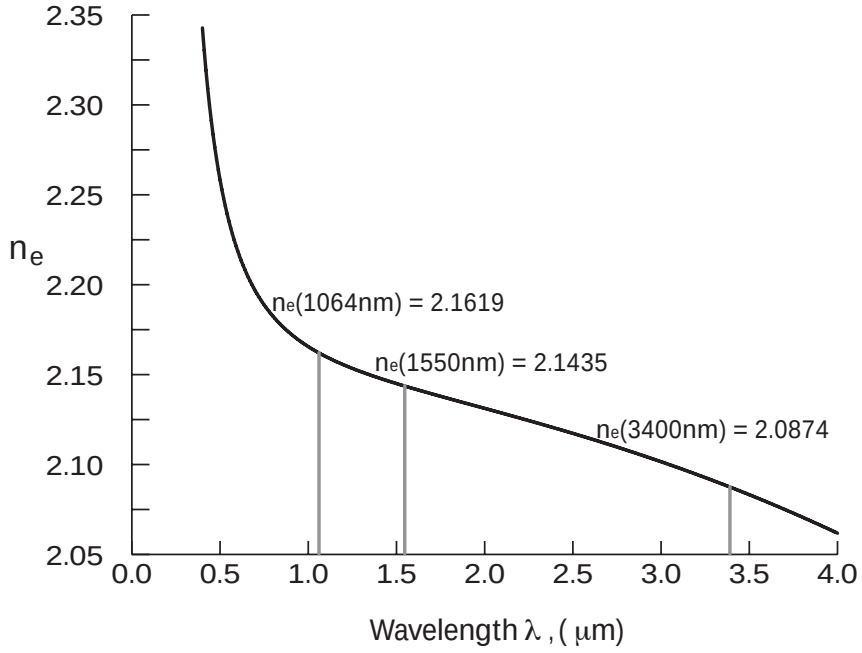

Figure 4.2: Extraordinary refractive index of $LiNbO_3$ at 150^oC as predicted by the Sellmeier equations derived by Jundt

the room temperature length due to thermal expansion. The room temperature grating period must be obtained by Equation 4.4, yielding the result $\Lambda_{g25^0C} = 29.47\mu m$.

Based on these calculations, a MgO:PPLN crystal was purchased from HC Photonics Corporation, containing six different grating domains, of various periods. The gratings periods were (28.76, 29.3, 29.86, 30.46, 31.1, 31.78)μm. The crystal was anti-reflectance coated for the pump, signal and idler at wavelengths of 1064, 1550 and 3400nm respectively.

4.4 Threshold Calculation

4.4.1 Mode Matching

A major factor influencing the threshold behavior of an OPO relates to the relative sizes of the interacting beams. A relationship exists between the spot sizes of the pump beam and the cavity mode (signal beam in this case) to ensure optimum overlap of the beams and hence, maximum pump depletion. The expression for the threshold pump power assuming the beams are closely approximated by focused Gaussian beams follows in Equation

$$(P_p)_{th} = \frac{\epsilon_0 n_s^2 n_p c \lambda_p^2}{8\pi^2 d_{eff}^2 L^2 (1-\delta^2) K^2}(1 - R_s) \tag{4.6}$$

where K^2 is the near field gain reduction parameter defined in Equation , accounting for the relative beam sizes and hence their degree of overlap.

$$K \frac{w_s w_i w_p}{w_s^2 w_i^2 + w_s^2 w_p^2 + w_i^2 w_p^2} \tag{4.7}$$

where w_j is the $\frac{1}{e^2}$ radius of the jth beam.

The optimal overlap of the pump and signal beams can be shown to be when the spot

sizes are in the ratio $w_s/w_p = \sqrt{(2)}$. The pump beam should therefore be appropriately focused such that the waist of the cavity mode, and the pump beam at the crystal are in this optimum ratio.

4.4.2 Crystal Length

The nonlinear gain and hence pump threshold power are strongly dependent on the length of the nonlinear crystal. For this project, the crystal was intended to serve a dual purpose. Firstly, as the gain material for the OPO described in this thesis. It is also possible to pursue an alternative means of creating the tunable light source, through the design of a parametric amplifier. The ideal crystal length for each of these devices is different. To enable efficient conversion in the OPO at high pump powers, a high pump threshold and therefore a short crystal is required. Contrarily, the single pass parametric amplifier requires a long crystal to increase the gain of the device. The crystal length of 10mm was chosen as a compromise which would enable satisfactory performance of each device.

It was deemed that the design of the OPA was not possible within the timespan of this project, and it has been left for future work.

Chapter 5: Results

5.1 Cavity

The synchronous pumping condition for a SPOPO requires that the round trip time for a resonant pulse in the cavity is equal to the time between successive pump pulses. This implies a strict relationship between the repetition rate of the pump laser and the cavity length of the OPO. In this case, the pump laser produces 13ps pulses at a repetition rate of 28.4MHz, implying that the total round trip cavity length of the OPO is equal to $c/28.4MHz = 10.556m$. This condition must be met to enable resonance, and hence is a fundamental issue for the cavity design.

The size of the available optical bench prohibited a simple linear cavity. Ring cavities are favorable for cases where internal loss due to far from ideal mirrors are an issue as a pulse is reflected off each mirror only once per round trip, however they are problematic in terms of maintaining angular alignment with a change in cavity length. Furthermore, a ring cavity would require two focusing sections to improve the stability of the cavity mode. A gamma cavity is essentially a linear cavity design in which the arms of the resonator have been folded. This configuration offers a compromise, as a greater number of mirrors results in a higher cavity loss, however it is space efficient and avoids problems associated with ring cavity alignment. The cavity alignment used is depicted schematically in Figure 5.1.

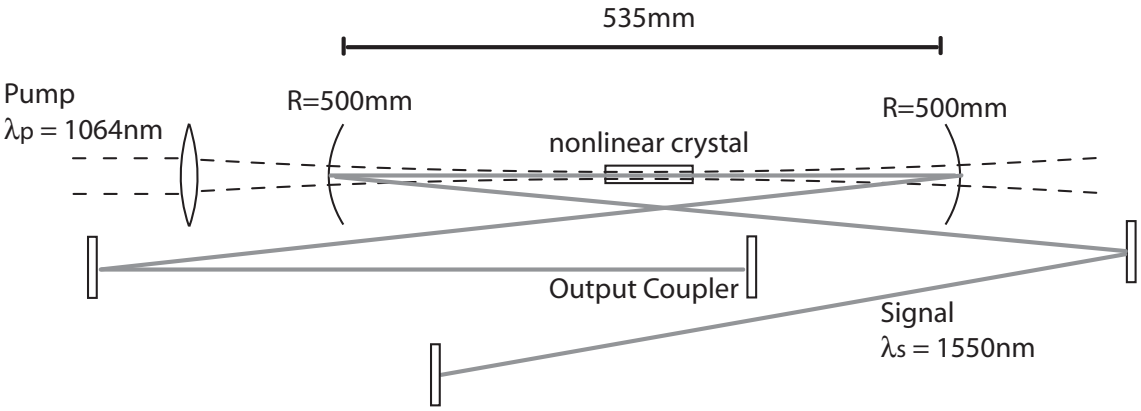

Figure 5.1: Schematic of gamma cavity configuration used for the SPOPO. The round trip cavity length is 10.556m

The focusing section of the resonator cavity was formed by two curved mirrors with a 500mm radius of curvature. The cavity was modeled by a simple linear cavity in which the mirrors were replaced with lenses of equal focal length. The resonator system was

analysed using the standard ray transfer matrix, or ABCD matrix approach, as outlined in the Kogelnik and Li's [48] excellent review of resonators. It was found that for a resonant wavelength of 1550nm, a stable waist of radius $86\mu m$ was formed when the separation of the curved mirrors was 535mm. In this configuration the beam radius at the end of each arm is 1.02 mm. The large beam size at the end mirrors causes difficulties in the alignment of the cavity, the focusing section of the cavity was therefore lengthened to 540mm, to improve the angular tolerance of the mirror alignment, and thus the stability of the cavity. As can be seen in Figure 5.2(a), this has only a small effect on the waist radius.

The dependence on the focusing mirror separation of the beam waist radius at the central point of the cavity, and at the end of the resonator arms is shown in Figures 5.2(a) and (b) respectively.

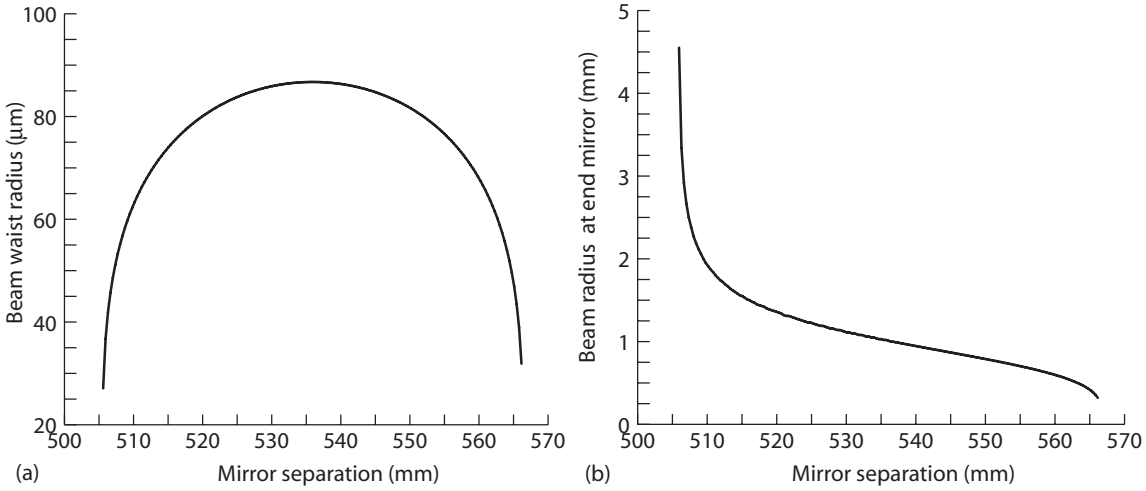

Figure 5.2: (a) Beam waist radius at the central point of the cavity and (b) beam radius at the end mirror of the resonator arms, as a function of the focusing mirror separation, as calculated using an ABCD ray transfer matrix program for a resonant wavelength of 1550nm

The arms of the oscillator were arranged such that the reflection angle off the face of the curved mirrors was as shallow as allowed by the crystal oven and housing. Furthermore, the length of each arm was equal (within $\sim 10cm$) to maintain a symmetric oscillator, preventing the beam from becoming elliptical. Three of the flat mirrors were high reflectors at the signal wavelength, and the fourth was nominally an output coupler ($OC\% = Tranmittance\%$). The output coupler mirror was mounted on a z-translation stage, allowing the cavity length to be tuned.

5.1.1 Cavity Mirrors and Coatings

In a singly resonant optical parametric oscillator, only one of the generated beams is resonant within the optical cavity. As is usually the case, in the design of this SROPO, the signal wave has been chosen as the resonant frequency. This condition can only be imposed by the mirrors forming the cavity, and thus the mirrors must be coated such that they have high reflectance at the signal ($\lambda_s = 1550nm$) and high transmittance at the pump and idler ($\lambda_p = 1064nm$ and $\lambda_i = 3.4\mu m$). In an ideal SRO, the cavity mirrors are 100% transmissive at the pump and idler frequencies and totally reflective at the resonant signal frequency.

Standard optical components used in the ultraviolet, visible and near-infrared regions of the spectrum are typically made from fused silica or similar glasses. Such materials typically have a transmission range from $\sim 200nm$ to $2.6\mu m$. At $2.9\mu m$ strong absorption occurs due to excitations of OH vibrational resonances. This makes fused silica optical components unsuitable for use in the OPO, as the idler wavelength lies beyond the transparency window. Calcium fluoride is often used as an optical substrate for components used in infrared optics as it has a transparency window from $150nm$ to $\sim 10\mu m$ and is free from vibrational absorptions. CaF_2 was therefore chosen as the optical material for the curved mirrors which form the focusing section of the OPO.

Coatings were required for the cavity mirrors to achieve high reflectivity at the resonant signal wavelength (1500nm) and low reflectivity at the pump and idler wavelengths ($1064nm$ and $3.4\mu m$) respectively. The mirrors were created on the CaF_2 optical substrate using the quarter-wave stack technique. Alternating layers of high-index and low-index materials are deposited in films of thickness equal to a quarter-wave optical length are deposited to create the mirror. Increasing the value of the refractive index ratio or the number of layer pairs increase the peak reflectance value.

Absorption due to -OH vibrational bands was also an issue for the HR coating for the CaF_2 mirrors. Initial trials using alternating layers of SiO_2 and HfO_2 resulted in films with strong absorption at $2.9\mu m$ and higher wavelengths, caused again by OH absorption. This is not an issue for the input coupling mirror as no power should be present in the idler beam at this point. Furthermore, these films exhibited very low reflectivity at the pump wavelength (1064nm) and hence was deemed suitable for coating the input coupling mirror. Eight layer pairs of HfO_2 : SiO_2 were deposited on the input mirror. The transmission spectrum of the coated mirror is shown in Figure 5.3.

Low idler transmission at the output mirror is however, undesirable as it results in a loss of idler output power. The coating for the idler output coupler was therefore designed using oxygen-free materials to avoid -OH absorption in the film. Magnesium fluoride and zinc sulphide were used as coating materials. Four layer pairs of MgF_2 : ZnS were deposited on the output curved mirror. The improved transmission at wavelengths at and beyond $2.9\mu m$ is evident in Figure 5.3.

It is evident from Figure 5.3, that ideal reflectivity at the signal wavelength was not achieved for either of the mirrors. Considerable problems were encountered with coating adhesion, limiting the number of layers which could be deposited without cracks forming. The coatings for the curved cavity mirrors were designed and deposited by Glen McCarthy, a member of LPC at RSPhysSE.

The transmittance of the curved cavity mirrors was measured using a Carey 5000 spectrophotometer. As is evident in Figure 5.3, the upper wavelength of the instrument's measurement range is $3300nm$, shorter than the proposed idler wavelength ($3.4\mu m$). The significant transmittance at the signal wavelength of $1550nm$ is evident in Figure 5.3.

The transmittance at the signal and idler wavelengths is not as crucial for the flat cavity mirrors, as it is assumed that almost all of the power in these beams will be lost at the first curved mirror. Therefore commercial broad band coatings centered at the signal wavelength were sufficient for these mirrors.

5.1.2 Pump Focusing

The size of the pump waist radius at the crystal is an important parameter in calculating the threshold for an OPO. Furthermore it is important to have knowledge of the

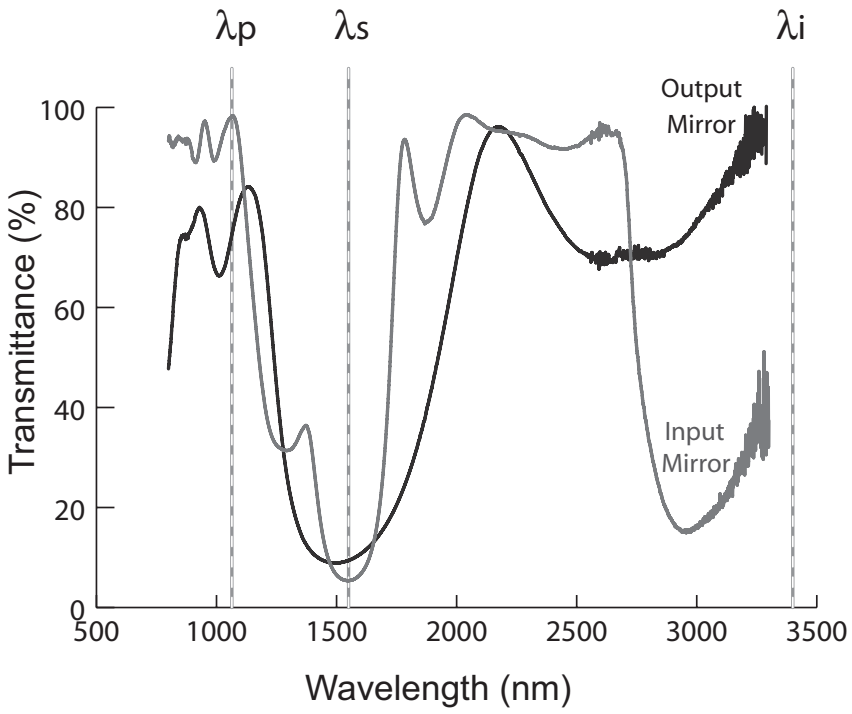

Figure 5.3: Transmittance spectrum of the cavity mirrors

pump beam quality in order to estimate the accuracy of theoretical models. A common measurement of beams is the so called M^2 beam-quality measurement. The M^2 parameter describes the propagation of the beam as in Equation 5.1, and hence quantifies the divergent behavior of the beam.

$$w(z) = w_0 \left[1 + \left(\frac{z\lambda M^2}{\pi w_0^2} \right)^2 \right]^{1/2} \tag{5.1}$$

where $w(z)$ is the beam radius as a function of the propagation distance z with respect to the focal plane, where the beam waist radius is equal to w_0. The parameter M^2 is equal to unity for diffraction limited Gaussian beams and increases for more divergent beams.

A measurement of the pump beam waist radius as a function of z about the focal plane (at the center of the resonant cavity) at low pump power was made using a beam profiler, measuring the beam diameter in the horizontal and vertical dimensions. A 300mm focal length lens was placed in the beam such that the focal plane of the pump was equidistant from the curved cavity mirrors and the pump beam diameter was roughly $\sim 100\mu m$ at that point. The data was fitted by Equation 5.1 using a least squares technique, to yield an estimate of the value of M^2 for the pump beam in the cavity, and the beam waist at the focal plane.

The M^2 values obtained from the fit to the data are $M^2_{Vertical} = 1.1$ and $M^2_{Horizontal} = 1.05$ for the vertical and horizontal directions respectively. These values are close to unity and hence, the beam is close to diffraction limited, and is well described by a focused Gaussian beam. The beam is slightly elliptical at its focus as indicated by the unequal beam waists in the vertical and horizontal directions, $w_{0Vertical} = 43\mu m$ and $w_{0Horizontal} = 37\mu m$ respectively. This is a known issue with the pump laser. A cylindrical

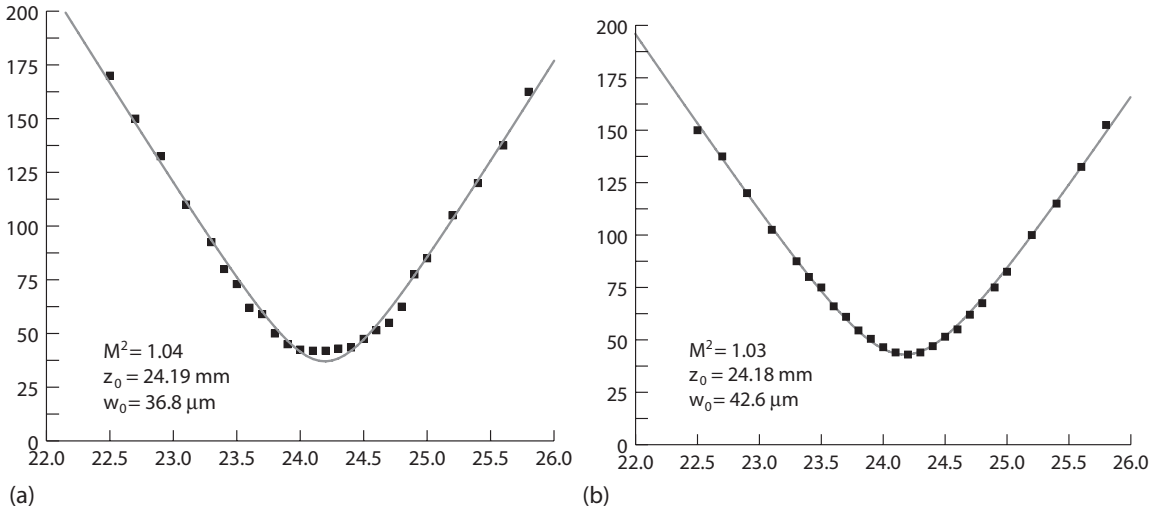

Figure 5.4: Pump beam profile for the (a) horizontal and (b) vertical dimension.

lens after the amplifier stage of the pump laser is employed to counter this effect, though a perfectly circular beam is still difficult to achieve in the current arrangement.

It is clearly observable that the data is fitted more accurately in the vertical than in the horizontal dimension. This is most likely due to aberrations caused in the amplifier stage of the pump laser and is consistent with previous observations and experience with the pump laser.

5.1.3 Alignment

The cavity was arranged on the optical bench as shown in Figure 5.1. The mirror separation and arm lengths were measured to the nearest millimeter. The alignment of the cavity mirrors was made possible by the visible second-harmonic beam at 532nm generated in the crystal. The cavity length however, must be accurate to within a few hundred microns for resonance to occur. The signal output coupling mirror at the end of the first arm was therefore place on a z-translation stage, such that the cavity length could be controlled on the order of a micron. The cavity length was tuned until resonance occurred, easily recognizable due to the presence of a red, visible beam at $\sim 630nm$, generated at the sum frequency of the pump and signal. This implies the presence of the resonant signal beam, which could be verified with a phosphorescent card or IR viewer.

5.1.4 Cavity Detuning

The behavior of the SPOPO with cavity-length detuning was examined. This was achieved by scanning the output coupling mirror on a z-translation stage and measuring the pump depletion and signal output power. The signal wavelength and bandwidth were also measured simultaneously using an OSA. The signal power as a function of the SPOPO cavity-length detuning is shown in Figure5.5.

The pump depletion and hence the signal power are not symmetric about zero cavity detuning. This is consistent with observations of McCarthy and Hanna [45] and Piskarskas [73]. Theoretical considerations of Cheung and Liu [56] suggest that this effect should be expected due to detuning-dependent phase-shift terms in the expression for the gain of a SPOPO.

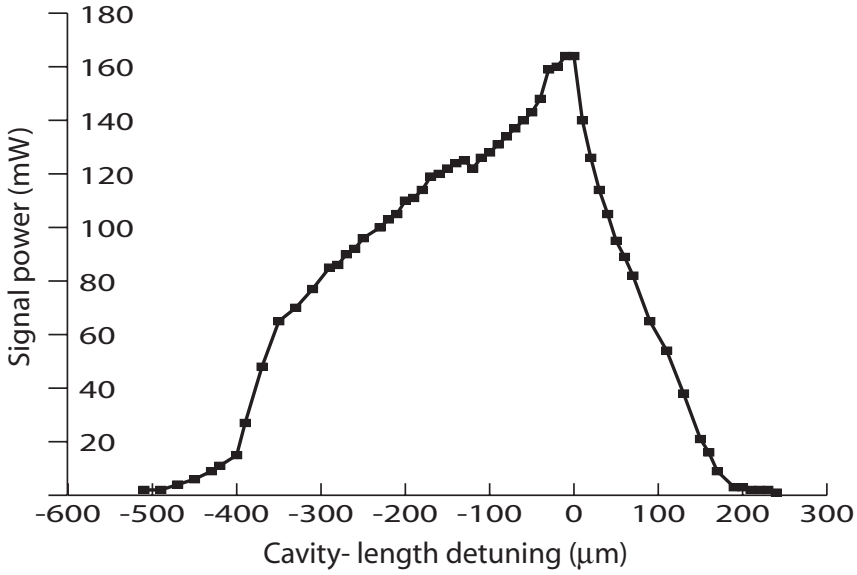

Figure 5.5: Variation in the average signal output power with SPOPO cavity-length detuning at a pump power of 10.1W

The signal wavelength and bandwidth as functions of the SPOPO cavity-length detuning are shown in Figure 5.6.

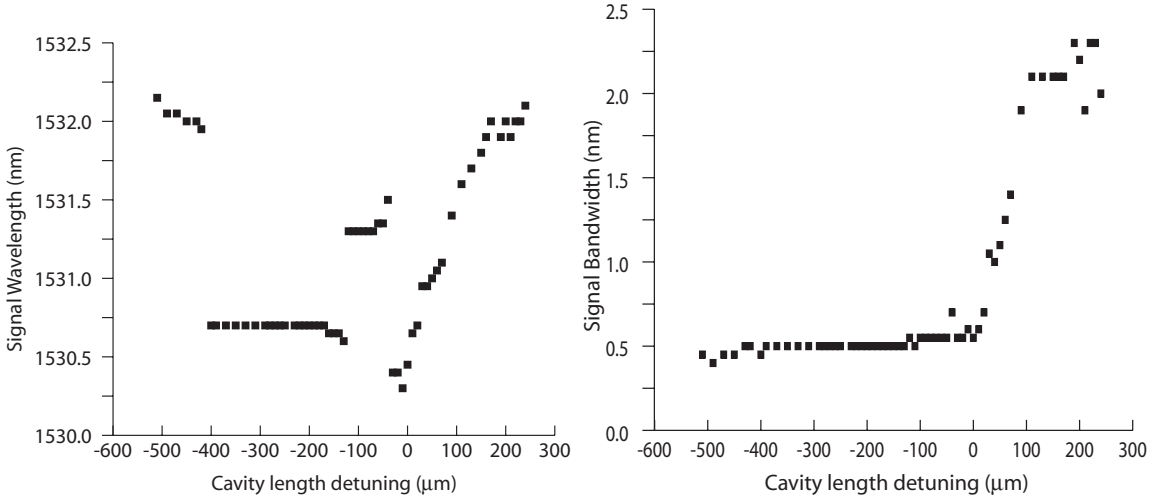

Figure 5.6: Variation in the (a) signal wavelength and (b) signal bandwidth with SPOPO cavity-length detuning at a pump power of 10.1W

The complex behavior of the OPO signal wavelength with cavity-length detuning is evident in Figure 5.6(a). The cluster structures observed in the signal spectrum are most likely caused by transverse mode competition. This can be attributed to the small pump spot size, causing the pump to couple to higher order transverse modes than the desired TEM_{00} mode. In addition, previous work involving picosecond OPO's, has shown that GVD has a significant effect on the detuning behavior [74]. Although a small effect on a single pass, GVD affects the resonant signal over multiple passes, causing a temporal broadening of the signal pulse, and a chirped pulse. This was not investigated further however, as it is beyond the required depth of this project.

The signal bandwidth is also non-symmetric about zero cavity-length detuning, exhibiting constant bandwidth at longer cavity lengths and a linear increase in bandwidth with cavity length for shorter cavities. This feature is common in all three of the cavity-length detuning relationships observed, as seen in Figures 5.5 and 5.6. The SPOPO cavity is in a more stable configuration when detuning to shorter cavity lengths, indicating the non linear interactions are more stable when the back of the signal pulse interacts with the front of the pump pulse, than in the converse scenario.

5.2 Temperature Tuning

The tuning parameters governing the phase matching condition, and hence the output wavelengths are dependent on the temperature of the nonlinear medium. Temperature control of the nonlinear crystal is therefore a simple and commonly used method for tuning the output of an OPO. This was achieved in this experiment by mounting the crystal in a brass holder making thermal contact with a crystal oven. The oven controller allowed the temperature to be tuned between room temperature and $\sim 250^oC$ (in increments of 0.1^oC). The OPO however, was not operated at temperatures much lower than 100^oC, in order to avoid photorefractive damage. A translation stage allowed the oven and crystal mount to be translated across the beam, to gain access to regions of the crystal with different grating periods.

An (Agilent 86142B) Optical Spectral Analyzer (OSA) was used to measure the wavelength of the signal beam. The upper wavelength limit for the OSA was $1700nm$ such that the idler wavelength could clearly not be measured with this instrument. The signal-output wavelength as a function of crystal temperature for various different grating periods is shown in Figure 5.7(a). The idler-output temperature tuning curves shown in Figure 5.7(b) were calculated from that of the signal, using the energy conservation condition.

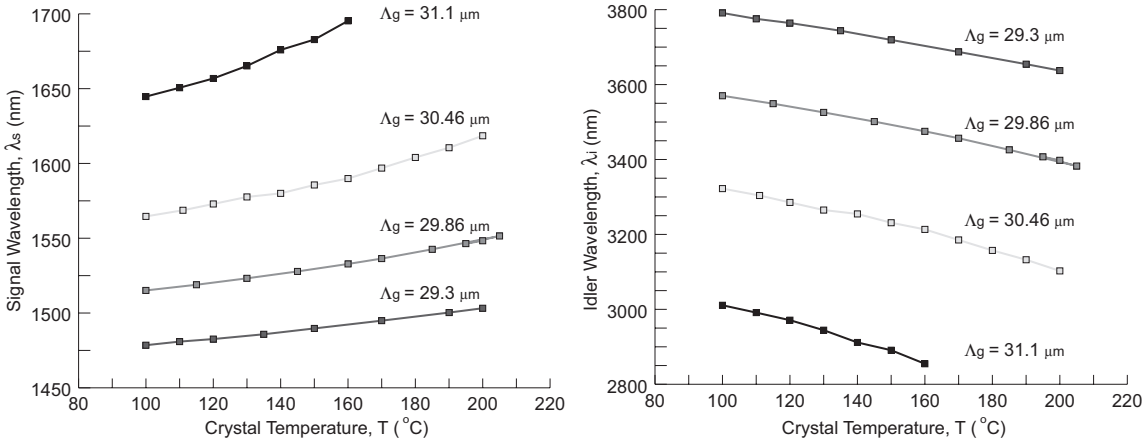

Figure 5.7: Temperature tuning curve of the PPLN OPO

5.3 Pump Depletion

The depletion of power from the pump beam is an important issue for OPO's. The power in the generated beams must, to conserve energy, be drawn from the pump beam, and thus maximizing pump depletion increases the overall conversion efficiency.

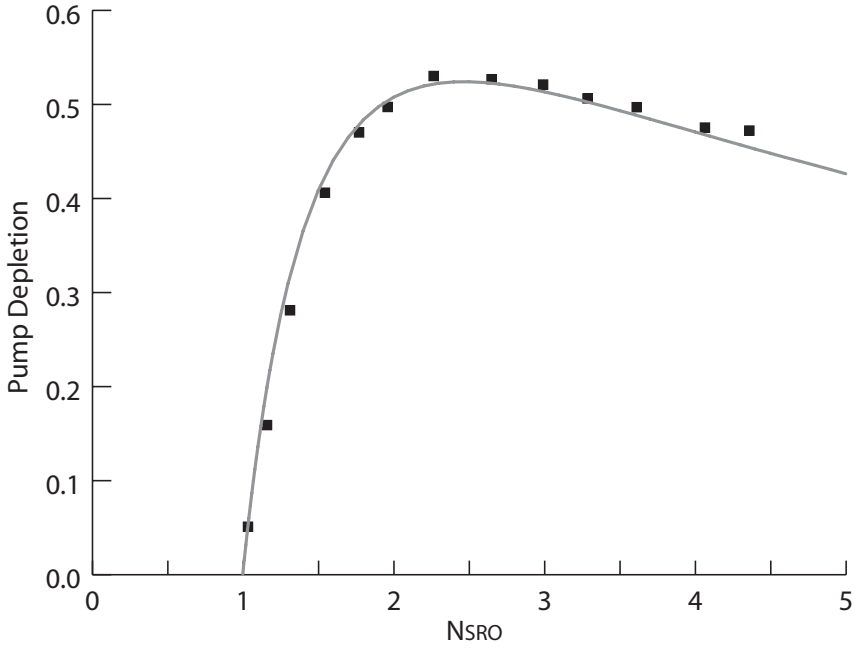

Figure 5.8: Pump depletion as a function of number of times above threshold (N_{SRO}) for the SPOPO with 30% output coupling. $P_{th} = 1.9W$, Depletion$_{MAX} = 52.5\%$.

Measuring the transmitted pump power when the oscillator is in and out of resonance allows the degree of pump depletion to be deduced. Figure 5.8 shows the pump depletion as a function of the number of times above threshold, measured for the SPOPO with a 30% output coupler as the end mirror for one of the resonator arms as in Figure 5.1. In this configuration, the pump threshold power was equal to $1.9W$ and the maximum pump depletion was 53%. The data was fitted using the plane wave model for conversion efficiency of Kreuzer [49], scaled using a least squares fit on the parameters of threshold power and maximum depletion.

5.3.1 Threshold

In order to obtain efficient conversion from the pump to the idler at high pumping powers, it is necessary to increase the pump threshold power. The pump threshold power can be increased by changing a number of different parameters, as is evident from the simple plane wave model for the pump threshold power given in Equation 5.2.

$$(P_p)_{th} = \frac{\epsilon_0 n_s^2 n_p c \lambda_p^2}{\pi^2 d_{eff}^2 L^2 (1-\delta^2)} (1 - R_s) A \tag{5.2}$$

where R_s is the reflectivity at the signal and A is the beam area. For a given crystal (fixed L and d_{eff}), the simplest ways of increasing the pump threshold power are by increasing the loss in the cavity (and thereby decreasing R_s) or increasing the beam area.

5.3.2 Cavity loss

Increasing the cavity loss is easily achieved by increasing the signal output coupling. The depletion as a function of pump power for various output couplers is shown in Figure 5.9. The expected increase in pump threshold power with increasing loss can clearly be seen.

This however, has an adverse effect on the maximum pump depletion which is observed to decrease.

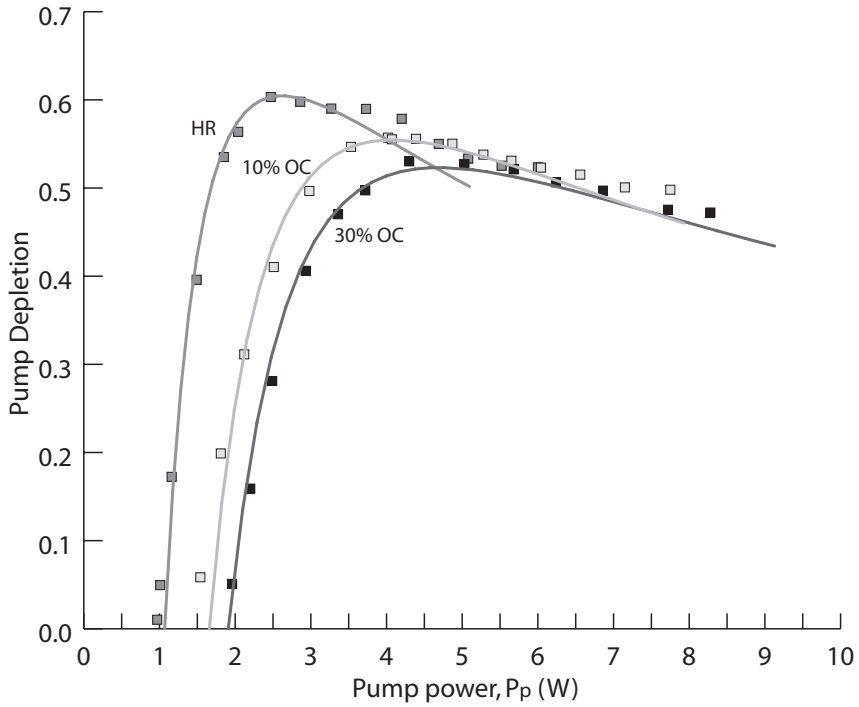

Figure 5.9: Pump depletion as a function of pump power for various levels of signal output coupling

The decrease in maximum pump depletion results in a decrease in the overall conversion efficiency, and is therefore undesirable. This implies that increasing the loss is not an ideal way to increase the pump threshold.

A simple model was constructed in an attempt to explain the observed behavior. An existing numerical model describing a single pass parametric oscillator for beams with Gaussian radial dependence was used. The results of this OPA model were applied to an OPO by constructing a simple model in which a fraction of the OPA output is recirculated at the input, thus creating a simple model for an OPO. This is shown in Figure 5.10

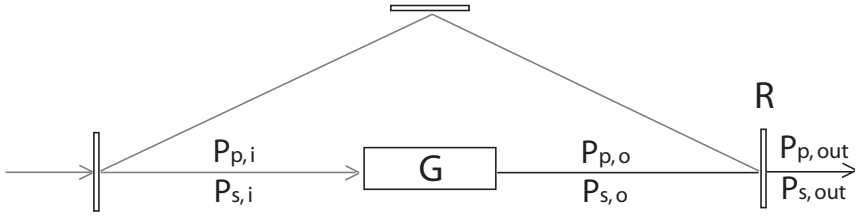

Figure 5.10: Simple conceptual model of an OPO

The pump depletion D is described by Equation 5.3.

$$D = \frac{P_{p,i} - P_{p,out}}{P_{p,i}} \tag{5.3}$$

The output signal power and the recycled signal power are related to the depleted

power of the pump by Equations 5.4 and 5.5.

$$P_{s,out} = (P_{p,i} - P_{p,out})\frac{\lambda_p}{\lambda_s} \tag{5.4}$$

where λ_p/λ_s defines the fraction of the depleted power which couples to the signal mode. Since $P_{s,o} = P_{s,out}(1-R)$, and $P_{s,i} = R \cdot P_{s,o}$ the recycled power can be given by Equation 5.5.

$$P_{s,i} = \frac{R}{(1-R)} D P_{p,i} \frac{\lambda_p}{\lambda_s} \tag{5.5}$$

Figure 5.11 shows a series of curves describing the pump depletion as a function of R (loss=1-R) for fixed input pump powers.

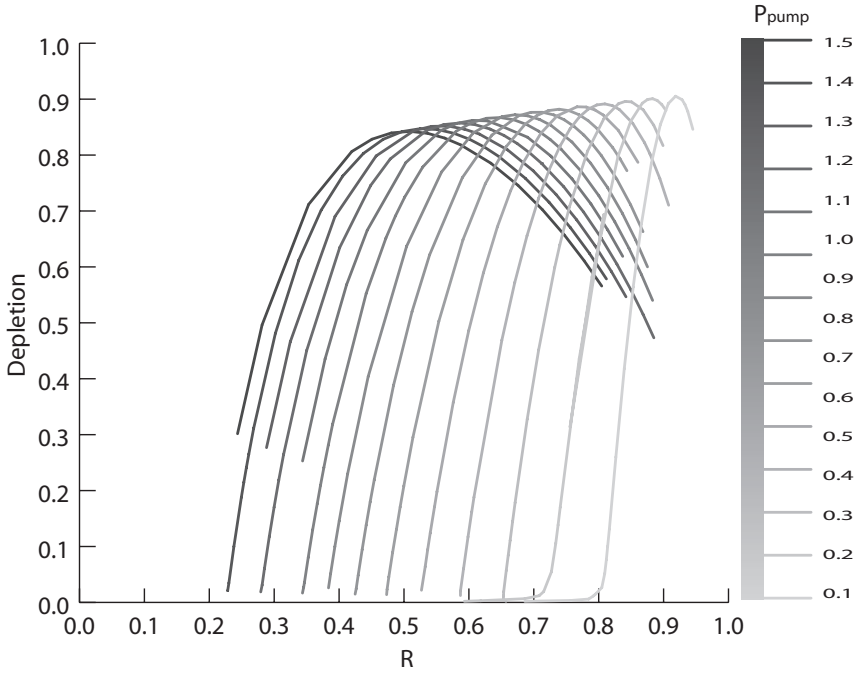

Figure 5.11: Pump depletion as a function of R for various pump input powers

The linear decrease in the maximum pump depletion with decreasing R (increasing loss) is clearly visible in Figure 5.11.

Data was accumulated for the pump depletion as a function of the input pump power for a fixed loss, corresponding to vertical sections in Figure 5.11. The results of this are shown in Figure 5.12.

Compared with the observed data in Figure 5.9, it is clear that this is not a numerically accurate model of the observed trend. Qualitatively however, the model predicts the same general trends as observed from the data and hence provides an adequate description of the observations. This model supports the argument that the high internal loss of the cavity will cause a decrease in the maximum depletion and hence the external conversion efficiency.

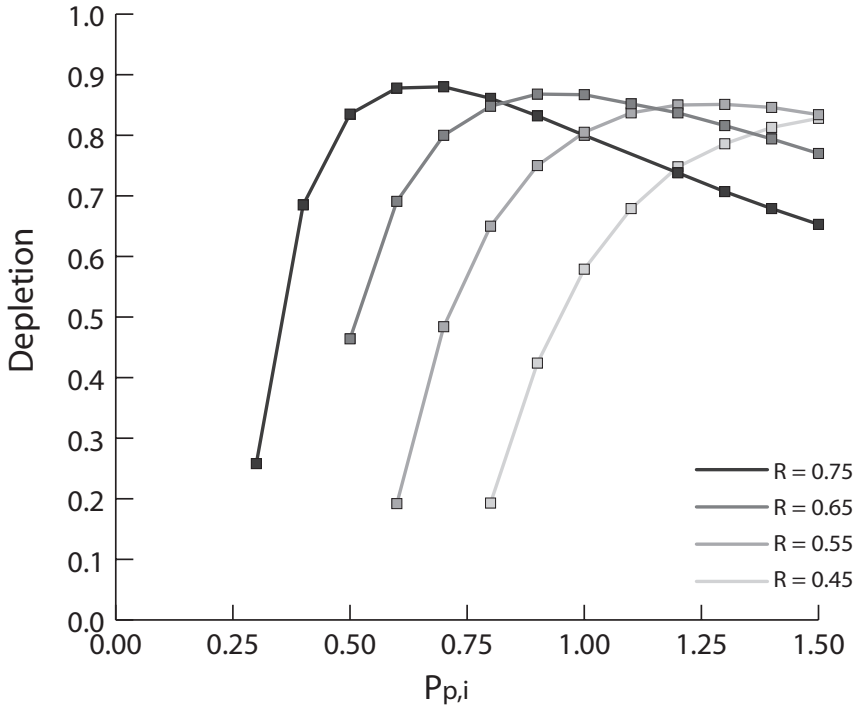

Figure 5.12: Pump depletion as a function of pump input power for fixed loss (values of R)

5.3.3 Beam Area and Mode Matching

Alternatively, the pump threshold power can be increased by increasing the size of the pump spot at the crystal. This alone however, will not greatly increase the gain. It is necessary to increase the size of the cavity mode (signal beam) commensurately with that of the pump to maintain the optimum overlap which occurs when $w_s = \sqrt{2}w_p$. A second pair of curved cavity mirrors with $1m$ radii of curvature were purchased, with the intention of increasing the cavity mode waist. Unfortunately, problems were encountered whilst trying to coat these mirrors, making this impossible within the timespan of this project.

It is however, the size of the interacting beams in the crystal, not at the beam waist which is of importance. It is therefore possible to increase the effective size of the cavity mode (signal) by shifting the crystal out of the focal plane such that the beam radius is greater. The pump beam focal plane can then be shifted in order to achieve the optimum overlap between the interacting beams. The pump spot was enlarged from its original size of $\sim 40\mu m$ radius to $\sim 100\mu m$ radius by changing the pre-cavity pump beam optics. Figure 5.13 shows the effect on the pump threshold and maximum pump depletion.

The pump threshold power was observed to increase by a factor of ~ 3 due to the increase in the spot size of the pump and resonant signal mode. Calculations of the near field gain reduction parameter K^2, for both the $40\mu m$ and $100\mu m$ pump beam radii, predict an increase in the pump threshold by a factor of 2.5, in reasonable agreement with the observed factor of 3 increase.

The crystal was shifted $\sim 20mm$ out of the focal plane along the propagation axis toward the input mirror in order to increase the size of the cavity mode at the crystal and tuned for maximum depletion, such that optimum overlap between the pump and signal could be achieved. Figure 5.14 shows the signal beam radius calculated using an ABCD

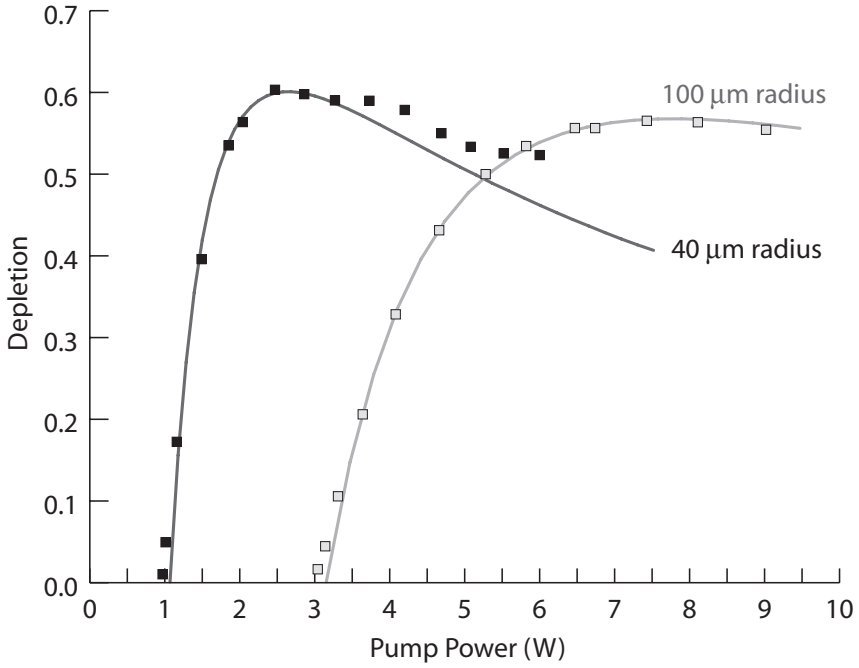

Figure 5.13: Pump depletion as a function of transmitted pump power for different pump spot-sizes

ray transfer matrix program. The optimum overlap between the pump and signal beams, $w_s = \sqrt{2}w_p$ occurs 21.8mm out of the focal plane for a $100\mu m$ pump beam waist radius.

The maximum pump depletion achieved decreased from 60% to 57%. The increase in pump theshold power is larger than that achieved by increasing the cavity loss. Furthermore, the conversion efficiency cost, arising from decreased pump depletion is modest when compared with that incurred by increasing the cavity loss.

5.3.4 Internal Loss

Measuring the pump threshold power as a function of the losses due to the output coupler allows an estimate of the internal loss of the cavity to be made. This measurement was performed in two different cavity configurations.

The first cavity design injected and extracted the pump to and from the cavity using two mirrors at 45^o, within the optical cavity. These mirrors were coated for HR at 1064nm for a 45^o reflection. These mirrors however, were not perfectly transmissive at the signal wavelength. Some losses occur at these mirrors, contributing to the internal loss of the cavity. The additional loss at the signal wavelength (1530nm during this particular measurement) due to the mirrors was measured to be 1.5% at each mirror. Figure 5.15(a) shows the threshold as a function of the loss for this cavity configuration.

In the second cavity design, the pump entered and left the cavity through the curved mirrors, and thus no additional intra-cavity optics were contributing to the internal loss of the cavity. Figure 5.15(b) shows the threshold as a function of the loss for this cavity configuration.

In Figures 5.15(a) and (b), the zero-threshold point on the linear fit to the data corresponds to the internal loss of the cavity. As described earlier, the internal loss in (a) is slightly higher due to the two intra-cavity mirrors. Correcting for this loss of 1.5% per mirror, the estimate of the internal loss is 34.6%. This agrees with the value obtained

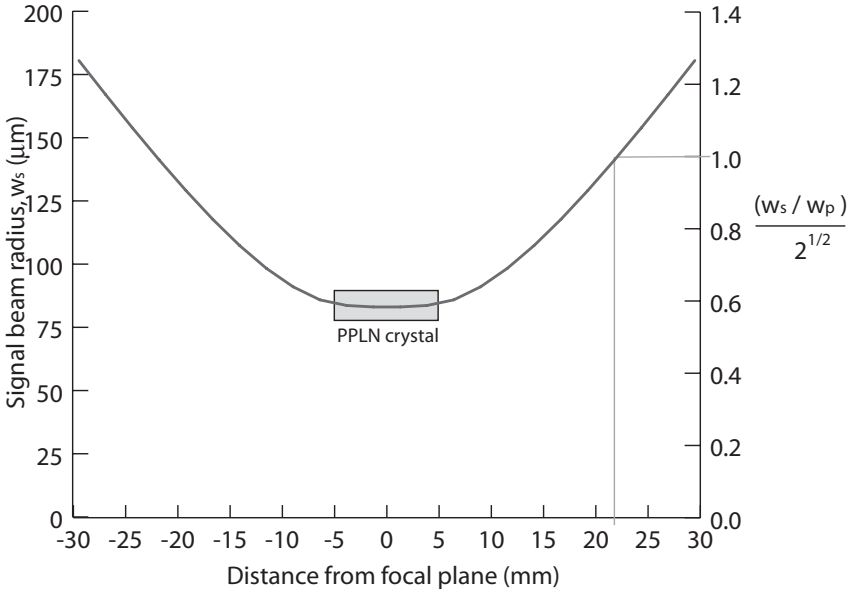

Figure 5.14: Calculated cavity mode (signal) radius as a function of displacement from focal plane. The right axis show the optimum overlap ratio, $\frac{w_s}{w_p\sqrt{2}}$ calculated for a $100\mu m$ pump beam radius.

from (b) of 34.5% internal loss.

The significant loss at the curved cavity mirrors described in Section 5.1.1, accounts for the majority of the internal loss of the OPO. The losses at the signal wavelength at the input an output focusing mirrors are $\sim 5.5\%$ and $\sim 9.5\%$ respectively. Two reflections occur at each mirror per round trip, resulting in a round trip loss contriubtion of $\sim 27\%$. The additional internal loss can be attributed to losses at the high reflecting mirrors, and at the crystal faces.

5.4 Idler Beam

The idler output beam was extracted from the OPO via the curved output mirror. From the transmission spectrum for this mirror shown in Figure 5.3, it can be expected that more than 80% of the power generated at the idler frequency be extracted from the cavity.

The divergent beam was focused using CaF_2 optics. The output of the OPO contains many collinear beams of different wavelengths, including the pump (1064nm), signal (1550nm) and idler ($3.4\mu m$), the second harmonic of the pump frequency (532nm), and the sum frequency generated beam of the pump and signal beams (631nm). These different collinear beams were split using a LiF prism, as LiF has a transparency window from 120nm to $6\mu m$, resulting in minimal losses at the idler frequency. The refractive index of LiF at $3.4\mu m$ is $n = 1.36$, so reflective losses are also low at the prism interface. Gold coated mirrors were used to transport the beam, such that the focal pane of the idler beam was $\sim 2m$ from the output mirror, at a convenient point on the optical bench for taking measurements.

The transmitted idler output power was measured as a function of the transmitted pump power, the results are displayed in Figure 5.16. The function has been fitted by the plane wave model conversion efficiency function of Kreuzer [49]. The maximum pump depletion was assumed to be 58% as is typical for this configuration. It was assume that

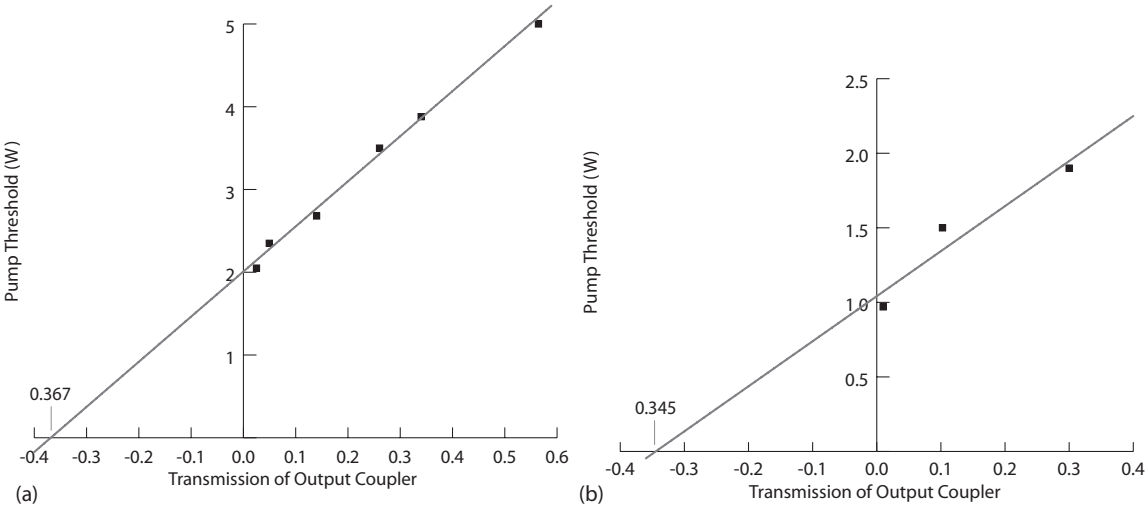

Figure 5.15: Pump threshold power as a function of the signal output coupling for two different cavity configurations

only 70% of the idler beam can be extracted from the cavity, due to losses at the cavity mirrors, CaF_2 lens, gold mirrors and LiF prism.

5.4.1 Beam Quality

The intensities achievable in the idler beam are of interest in regards to ablation experiments, and hence the beam was tightly focused using CaF_2 optics. The idler beam was characterized by a beam profile and a spatial profile of the spot in the focal plane. The beam profiler available was not sensitive to long wavelength radiation such as the $3.4\mu m$ idler beam. A straight edge was therefore scanned across the beam, and the transmitted power as a function of the edge position was measured using a calorimeter power meter. The resulting power distribution is the integral of the the idler beam spot profile. Differentiating the data would provide the spatial power distribution of the idler beam. The data was however, fit with the integral function of a Gaussian profile, using a least squares method. The $1/e^2$ beam radius was obtained from the fit. This measurement was performed for both the horizontal and vertical beam dimensions near the focal plane using an xyz-translation stage. The results of a single scan and the Gaussian integral function fit for one such plane are shown as an instructive example in Figure 5.17.

Similar results were obtained at various planes perpendicular to the beam propagation direction, the results of which were collated to allow the beam profile to be visualized as in Figures 5.18(a) and (b). The idler beam quality was described quantitatively by the M^2 parameter, by performing least squares fits of Equation 5.1 to the data from the horizontal and vertical dimensions of the beam.

The fitting parameters for the horizontal beam were ($z_0 = 10.94mm$, $w_0 = 53.9\mu m$, $M^2 = 1.56$), and those for the vertical, ($z_0 = 6.23mm$, $w_0 = 50.1\mu m$, $M^2 = 1.50$). These results show some degree of astigmatism is present as can be seen by the displacement between the focal planes in the horizontal and vertical dimensions. The beam quality parameter M^2 is not far from unity, hence the idler beam is well described by a focused Gaussian TEM_{00} mode. The minimum spot size is very close to $55\mu m$ circular spot. Idler powers of 1.5W at $3.35\mu m$ were achieved when pumping the OPO with 10W at 1064nm. This corresponds to an irradiance of $0.2GW/cm^2$.

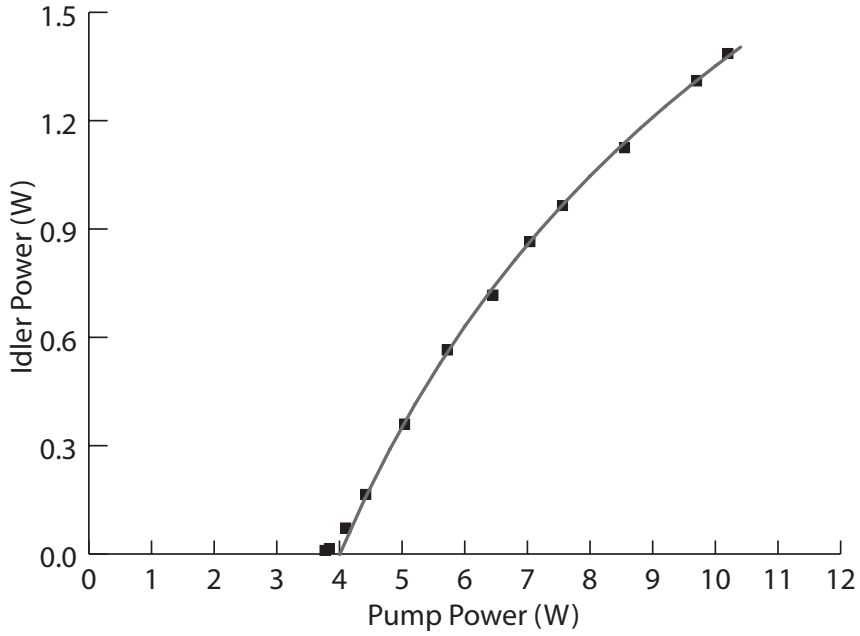

Figure 5.16: Transmitted idler power as a function of transmitted pump power.

5.5 Absorption Spectroscopy

The aim of this project was to produce a coherent light source at wavelengths capable of exciting vibrational resonances of C-H bonds in polymers. The strong coupling of energy from the idler beam to such resonances results in strong absorption at the resonant frequency. It is therefore possible to use the idler beam to perform a spectroscopic analysis of particular polymers. Conversely, the observation of resonant peaks at specific wavelengths acts as verification that vibrational excitation is occurring.

Placing a thin sheet of plastic in the path of the idler beam at the focal plane provided a simple verification of such absorption occurring. The plastic is melted in the path of the beam, a clear indication of strong absorption. Polyethylene strongly absorbed around $3.4\mu m$ which corresponds to the C-H stretching mode as expected. Simple plastic sheets however were not suitable for the spectroscopy experiment, as the strong absorption lead to melting.

The problem was solved by spin coating a thin layer of polycarbonate onto a silicon wafer. The silicon wafer acted as a heat sink, preventing the polymer film from melting. The polycarbonate films had an average thickness of $15\mu m$. The signal wavelength was monitored with an OSA from which the idler wavelength was inferred, whilst the crystal temperature was varied to tune the signal wavelength. Figure 5.19 shows the absorption spectrum of the polycarbonate film and silicon wafer. An averaged background spectrum has been used to normalize the data.

A strong absorption peak centered at $3.36\mu m$ was observed, again corresponding to -CH stretching modes which in general, resonate in the region 3050-3500nm. Unsaturated -CH modes resonate at higher frequencies than saturated -CH modes. The resonant wavelength of this vibrational mode, $3.36\mu m$ appears to be consistent with an unsaturated -CH mode. The weaker periodic structure at shorter wavelengths which is observed in Figure 5.19, are caused by multiple reflections in the silicon wafer.

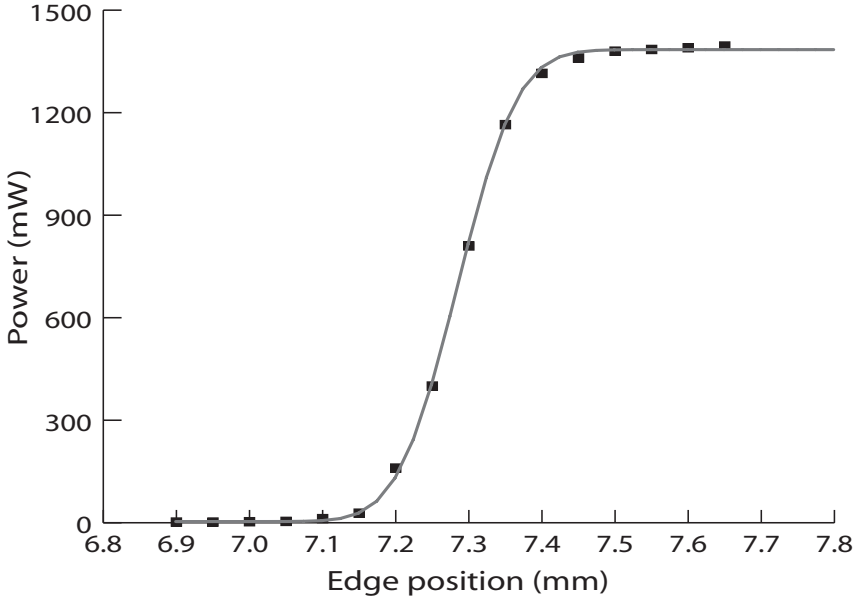

Figure 5.17: Transmitted power as a function of edge position. This data was measured for the horizontal beam dimension $\sim 10mm$ from the focal plane. The data has been fitted with the integral of a Gaussian function.

5.6 Machining Polymers

The focused idler output from the SPOPO was used to machine a pattern into a polymer sheet. The SPOPO was pumped at 10W, producing $\sim 1.5W$ of extracted idler power at the operating wavelength of $3.32\mu m$. This was focused to a spot size on the order of $50\mu m$ diameter. A set of gold scanning mirrors were attached to an x-y mirror scanner. The scanner was computer controlled by a program written by Darren Freeman, a member of LPC at RSPhysSE, allowing arbitrary patterns to be written. The title of this project was chosen as the pattern, the results of which can be seen in Figure 5.20. The angular scanning speed of the mirrors was such that the linear scanning speed at the focal plane, where the target material was located, was 2mm/s. Both perspex and polycarbonate targets were used.

Figure 5.21 shows a groove machined into solid perspex by the focused idler beam. The walls of the trench are smooth, a characteristic commonly observed in ablated structures, and do not show raised ridges characteristic of melting. The bubble-like structure visible on the floor of the trench however, are characteristic of melting having occurred. A slightly darkened region exists in the material beyond the edge, probably caused by heating effects.

The results of machining experiments with a solid polycarbonate target can be seen in Figures 5.22 and 5.23. The bubbled, fluid-like appearance of the machined region in Figure 5.22, is a clear sign that melting has occurred. A much darker heat-effected band is seen in Figure 5.23.

Regardless of the mechanism involved (ablation or evaporation), in some experiments the material has been removed from the sample as in Figure 5.21, indicating that the a vapor has indeed been formed. Analyzing the composition of the vapour plume however has been deemed to be out of the scope of this project, and has been left for future work.

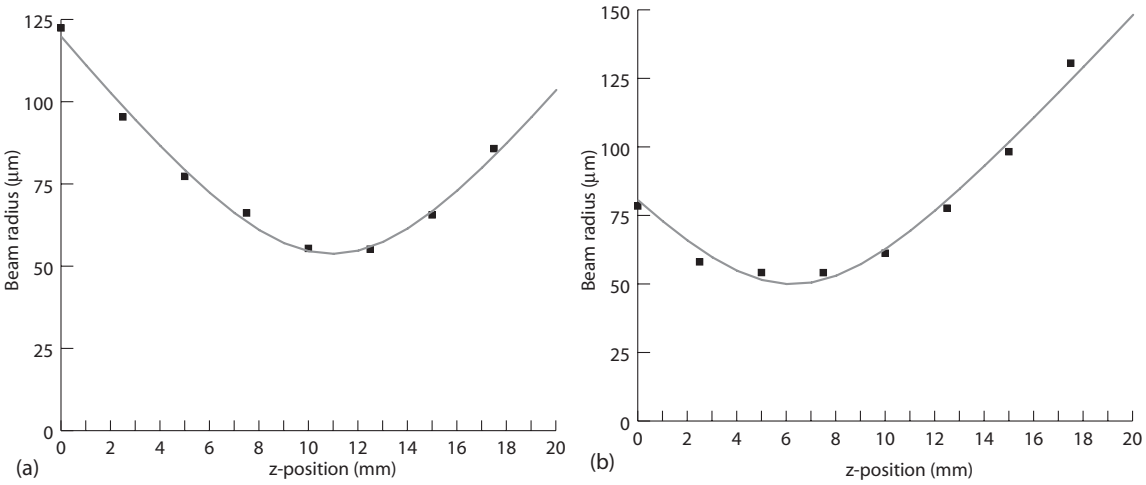

Figure 5.18: Idler beam profile in the (a) horizontal ($M^2 = 1.56$) and (b) vertical ($M^2 = 1.50$) dimensions.

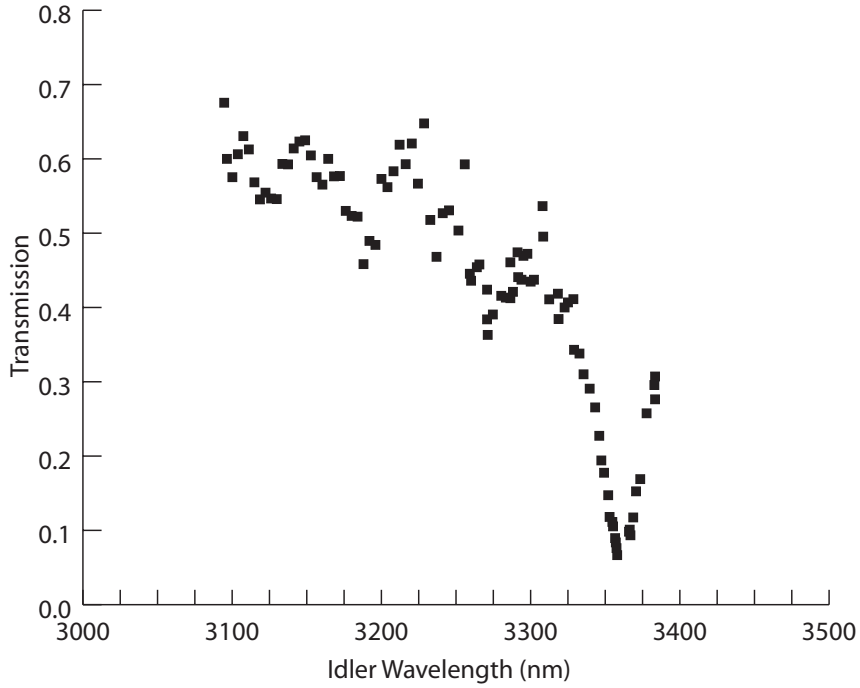

Figure 5.19: Absorption spectrum of a polycarbonate film deposited on a silicon wafer. A -CH resonance is observed, centered at $3.36\mu m$.

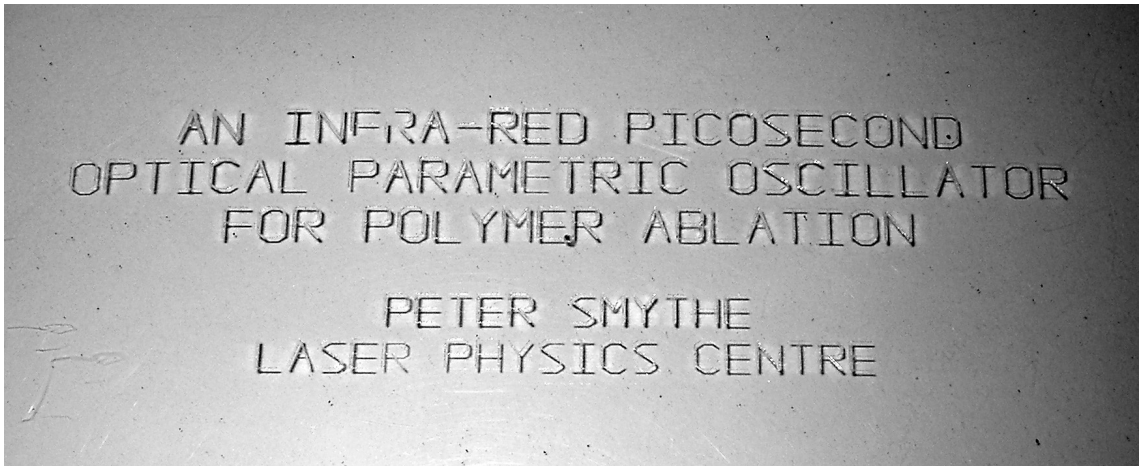

Figure 5.20: Photograph of machined writing in a polycarbonate target.

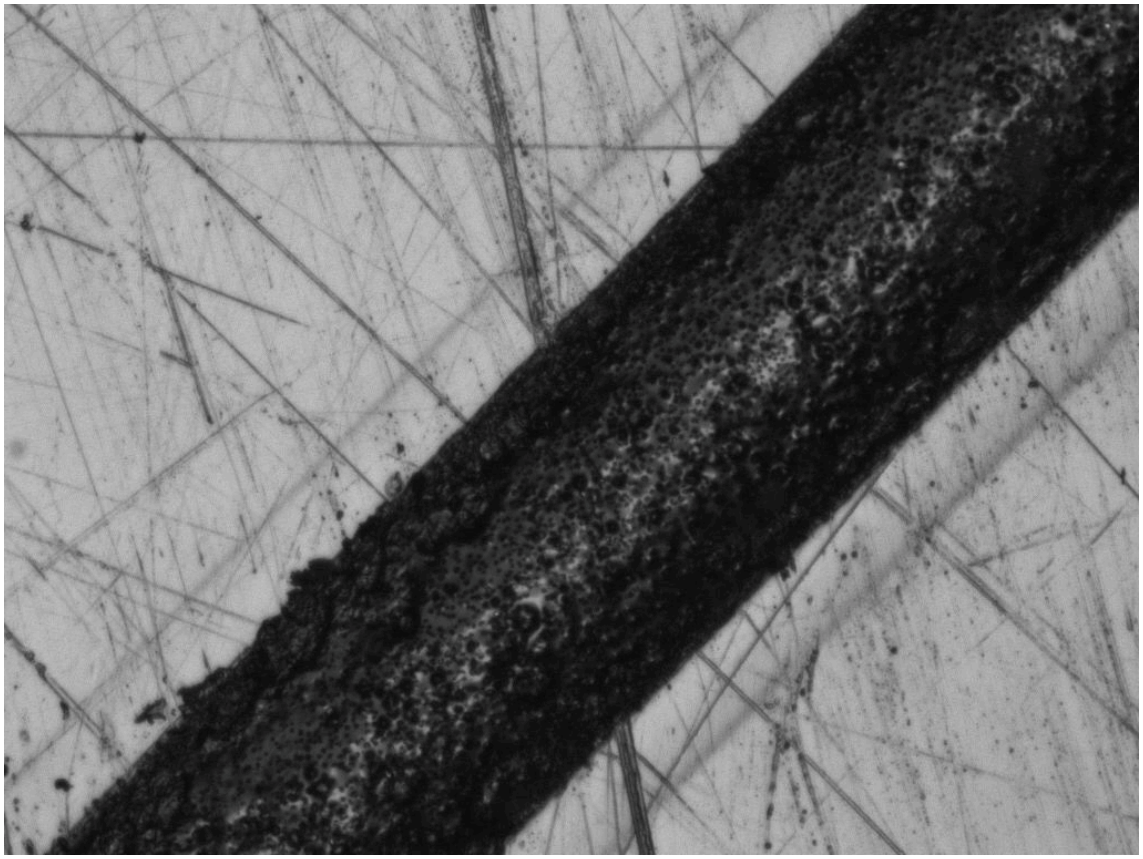

Figure 5.21: Photograph of machined perspex target. The field of view width is 1mm

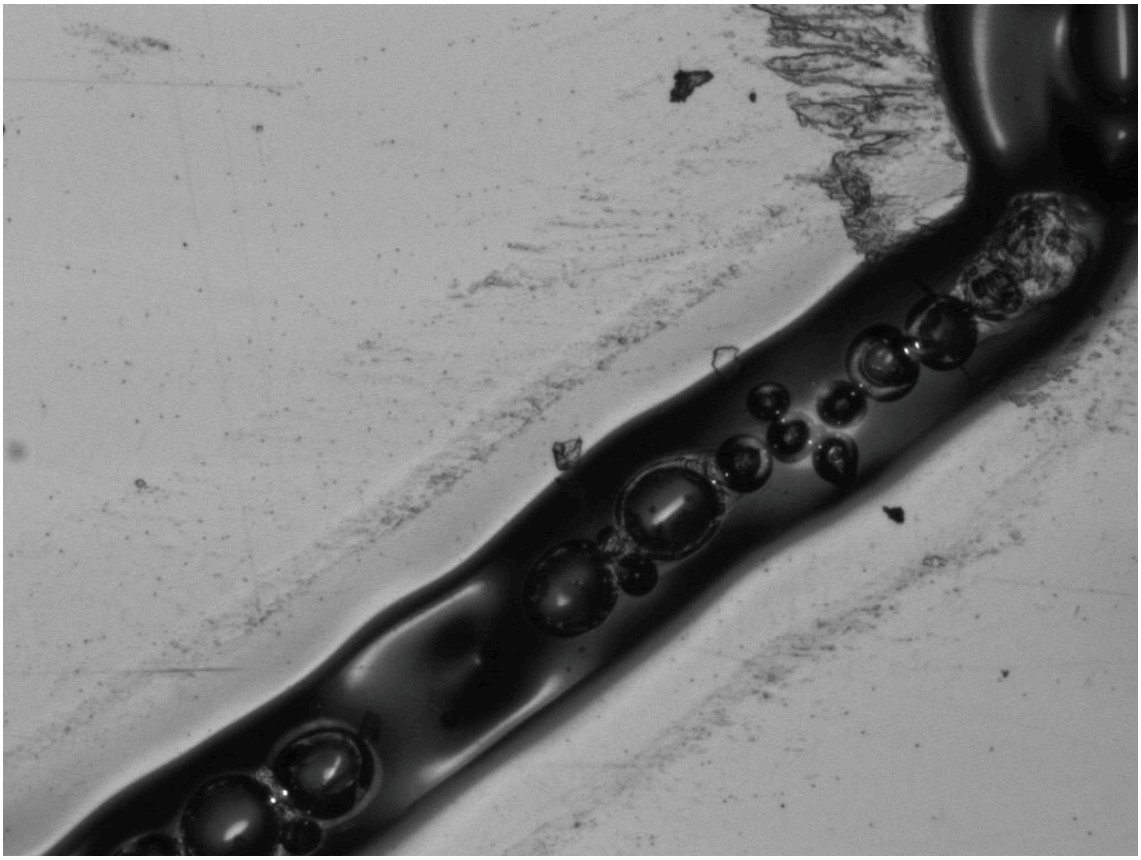

Figure 5.22: Photograph of machined polycarbonate target. The field of view width is 1mm

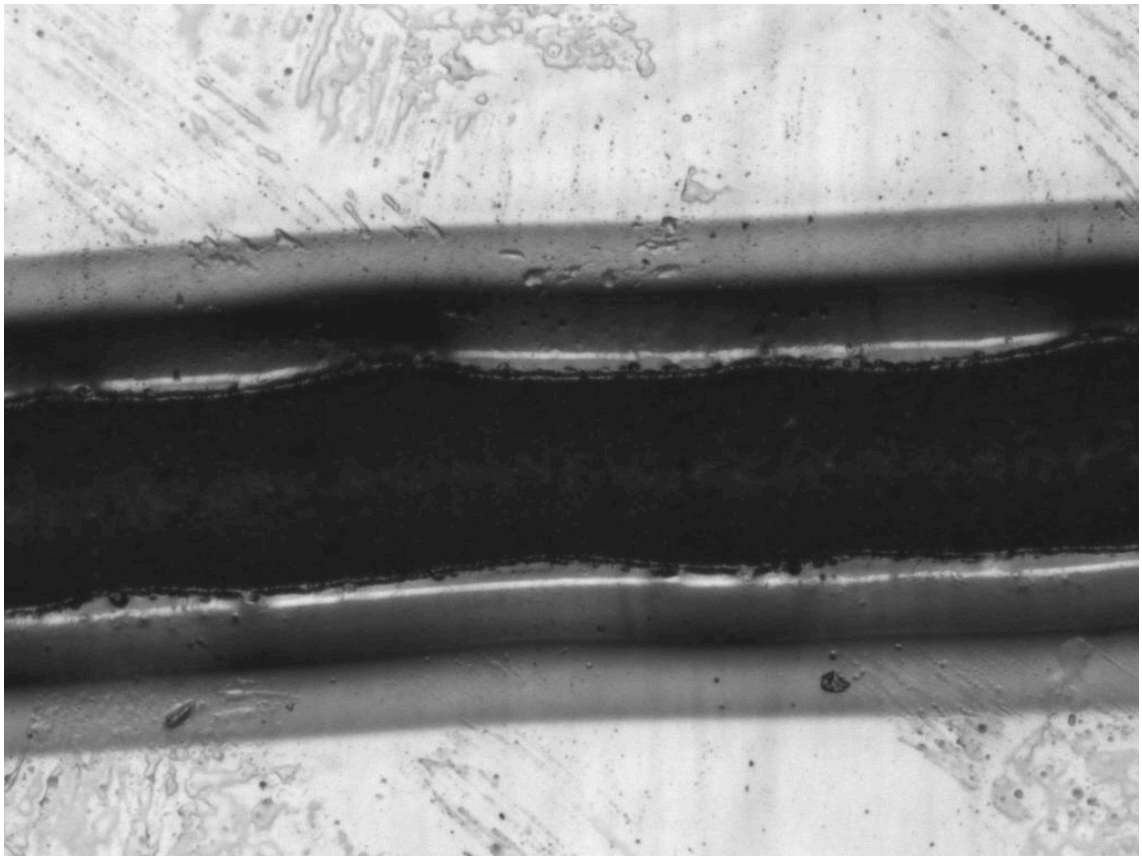

Figure 5.23: Photograph of machined polycarbonate target. The field of view width is 1mm

Conclusion

The generation of a light source suitable for pulsed laser ablation of polymers has been achieved. This was accomplished through the design and construction of a synchronously pumped optical parametric oscillator, based on magnesium oxide doped periodically poled lithium niobate. The OPO was pumped by a high average power, mode-locked Nd:YVO_4 laser, producing 13 picosecond pulses at a repetition rate of 28.4MHz. Consequently, the output of the OPO was a pulsed, coherent light source with considerable average power. The OPO generated radiation at the desired signal and idler wavelengths, centered at 1550nm and 3.4μm respectively. A wide tuning range was afforded by multiple grating periods of the PPLN crystal, and temperature control.

Absorption spectroscopy performed on a polycarbonate film showed the dramatic increase in absorption at wavelengths corresponding to vibrational excitations of C-H bonds, indicating that evaporation is initiated by the idler coupling to strong vibrational resonances. Preliminary experiments observing the machining of bulk polymers with the focused idler radiation were undertaken successfully.

This project has seen the successful development of an infrared picosecond optical parametric oscillator as a possible alternative to a free electron laser for pulsed laser polymer ablation. A great deal of future work is viable as a result of this initial study,which demonstrated the feasibility though the design of a prototype light source. The threshold of the OPO should be increased further by expanding the cavity mode size, using longer focal length cavity mirrors. A shorter crystal would also significantly increase the pump threshold power and allow for greater conversion efficiency at high average pump powers.

Bibliography

[1] J.S.Horwitz; J.Schou; P.M.Johansen; B.Toftmann; M.R.Papantonakis; R.C.Y.Auyeung; W.Kim; S.M.O Malley; D.M.Bubb and R.F.Haglund. UV and RIR matrix-assisted pulsed laser deposition of MEH-PPV films. *Thin Solid Films*, 453-454:177, 2004.

[2] G.B.Blanchet; C.R.Fincher and I.Malajovich. Laser evaporation and the production of pentacene films. *Journal of Applied Physics*, 94:6181, 2003.

[3] C.W.Tang and S.A.VanSlyke. Organic electrolumiscent diodes. *Appl. Phys. Lett.*, 51:913, 1987.

[4] F.Bender; R.W.Cernosek and F.Josse. Love-wave biosensors using cross-linked polymer wave guides on $LiTaO_3$ substrates. *Electronics Letters*, 36:1672, 2000.

[5] D.M.Bubb; J.S.Horwitz; J.H.Callahan; E.J.Houser; R.A.McGill; D.B.Chrisey; M.R.Papantonakis; R.F.Haglund.Jr; M.C.Galicia; and A.Vertes. Resonant infrared pulsed-laser deposition of polymer films using a free-electron laser. *Journal of Vacuum Science Technology A.*, 19:2698, 2001.

[6] R.A.McGill; R.Chung; D.B.Chrisey; P.C.Dorsey; P.Matthews; A.Piquè; T.E.Mlsna; J.L.Stepnowski. Performance optimization of surface acoustic wave chemical sensors. *IEEE Transactions on Ultrasonics, Ferroelectrics, and Frequency Control*, 45:1370, 1998.

[7] D.M.Bubb; J.S.Horwitz; R.A.McGill; D.B.Chrisey; M.R.Papantonakis; R.F.Haglund.Jr; B.Toftmann. Resonant infrared pulsed-laser deposition of a sorbent chemoselective polymer. *Appl. Phys. Lett.*, 79:2847, 2001.

[8] A.Piquè; R.A.McGill amd D.B.Chrisey. A new way to deposit organic thin films. *The Industrial Physicist*, 6:20, 2000.

[9] D.M.Bubb; R.A.McGill; J.S.Horwitz; J.M.Fitz-Gerald; E.J.Houser; R.M.Stroud; P.W.Wu; B.R.Ringeisen; D.B.Chrisey; R.F.Haglund.Jr. Effect of ablation parameters on infrared pulsed laser deposition of poly(ethylene glycol) films. *Journal of Applied Physics*, 91:9809, 2002.

[10] G.B.Blanchet and S.I.Shah. Deposition of polytetrafluoroethylene films by UV laser ablation. *Applied Physics Letters*, 62:1026, 1993.

[11] G.B.Blanchet. Laser ablation and the unzipping of addition polymer. *Journal of Applied Physics*, 80:4082, 1996.

[12] Y.Tsuboi and A.Itaya. Deposition of a thin polystyrene film by anthracene-photosensitized laser ablation at 351 nm. *Applied Physics Letters*, 74:3896, 1999.

[13] D.M.Bubb; M.R.Papantonakis; B.Toftmann; J.S.Horwitz; R.A.McGill; A.Piquè; and D.B.Chrisey. Laser-based processing of polymer nanocomposites for chemical sensing applications. *Journal of Applied Physics*, 89:5739, 2001.

[14] B.Roas; L.Schultz; G.Endres. Epitaxial growth of $YBa_2Cu_3O_{7-x}$ thin films by a laser evaporation process. *Appl. Phys. Lett.*, 15:1557, 1988.

[15] S.G.Hansen. Wavelength effects in the ultraviolet-laser ablation of polycarbonate and poly(α-methylstyrene) examined by time-of-flight mass spectroscopy. *Journal of Applied Physics*, 68:1968, 1990.

[16] D.M.Bubb; M.R.Papantonakis; J.S.Horwitz; R.F.Haglund.Jr; B.Toftmann; R.A.McGill; D.B.Chrisey. Vapor deposition of polystyrene thin films by intense laser vibrational excitation. *Chemical Physics Letters*, 352:135, 2002.

[17] L.V.Zhigilei; P.B.S.Kodali; B.J.Garrison. Molecular dynamics model for laser ablation and desorption of organic solids. *Journal of Physical Chemistry B.*, 101:2028, 1997.

[18] L.V.Zhigilei; E.Leveugle; B.J.Garrison; Y.G.Yingling; M.I.Zeifman. Computer simulations of laser ablation of molecular substrates. *Chemistry ReviewB.*, 103:321, 2003.

[19] M.Bass; E.W.VanStryland; D.R.Williams; W.L.Wolfe, editor. *Handbook of Optics*, volume II. McRaw-Hill, 1995.

[20] Y.R.Shen. *The Principles of Nonlinear Optics*. Wiley, 1984.

[21] A.Yariv. *Quantum Electronics*. Wiley, 1988.

[22] J.A.Armstrong; N.Bloembergen; J.Ducuing; P.S.Pershan. Interaction between light waves in a nonlinear dielectric. *Physical Review*, 127:1918, 1962.

[23] D.Kleinman. Nonlinear dielectric polarization in optical media. *Physical Review*, 126:1977, 1962.

[24] R.L.Sutherland. *Handbook of nonlinear optics*. Marcel Dekker, 1996.

[25] W.Brunner and H.Paul. Theory of optical parametric amplification and oscillation. *Progress in Optics*, XV:3, 1977.

[26] R.G.Harper and B.S.Wherret. *Nonlinear optics*. Academic Press, 1977.

[27] M.Bass; J.M.Enoch; E.W.VanStryland; W.L.Wolfe, editor. *Handbook of Optics*, volume IV. McRaw-Hill, 2001.

[28] J.D.McMullen. Optical parametric interactions in isotropic materials using a phase-corrected stack of nonlinear dielectric plates. *Journal of Applied Physics*, 46:3076, 1975.

[29] L. Goldberg; W. K. Burns; R. W. McElhanon. Difference-frequency generation of tunable mid-infrared radiation in bulk periodically poled $LiNbO_3$. *Optics Letters*, 20:1280, 1995.

[30] W.H.Louisell; A.Yariv; A.E.Siegman. Quantum fluctuations and noise in parametric processes. I. *Physical Review*, 124:1646, 1961.

[31] G.D.Boyd and A.Ashkin. Theory of parametric oscillator threshold with single-mode optical masers and observation of amplification in $LiNbO_3$. *Physical Review*, 146:187, 1966.

[32] G.D.Boyd and D.A.Klienman. Parametric interaction of focused gaussian light beams. *Journal of Applied Physics*, 39:3597, 1968.

[33] S.Guha; F.Wu and J.Falk. The effects of focusing on parametric oscillation. *IEEE Journal of Quantum Electronics*, 18:907, 1982.

[34] F.Bréhat and B.Wyncke. Calculation of double-refraction walk-off angle along the phase-matching directions in non-linear biaxial crystals. *Journal of Physics B: Atomic Molecular and Optical Physics*, 22:1891, 1989.

[35] D.A.Kleinman. Theory of second harmonic generation of light. *Physical Review*, 15:1761, 1962.

[36] Y.F.Chen and Y.C.Chen. Analytical functions for the optimization of second-harmonic generation and parametric generation by focused gaussian beams. *Applied Physics B*, 76:645, 2003.

[37] S.Guha. Focusing dependence of the efficiency of a singly resonant optical parametric oscillator. *Applied Physics B: Lasers and Optics*, 66:663, 1998.

[38] J.A.Giordmaine and R.C.Miller. Tunable coherent parametric oscillation in $LiNbO_3$ at optical frequencies. *Physical Review Letters*, 14:973, 1965.

[39] R. L. Byer; M. K. Oshman; J. F. Young; and S. E. Harris. Visible CW parametric oscillator. *Applied Physics Letters*, 13:109, 1968.

[40] R. L. Byer; A. Kovrigin and J. F. Young. A CW ring cavity parametric oscillator. *Applied Physics Letters*, 15:136, 1969.

[41] I.F.Elder and J.A.C.Terry. Efficient conversion into the near- and mid-infrared using a PPLN OPO. *Journal of Optics A: Pure and Applied Optics*, 2:19, 2000.

[42] T.Graf; G.McConnell; A.I.Ferguson; E.Bente; D.Burns and M.D.Dawson. Synchronously pumped optical parametric oscillation in periodically poled lithium niobate with 1-W average output power. *Applied Optics*, 38:3324, 1999.

[43] M.Sato; T.Hatanaka; S.Izumi; T.Taniuchi and H.Ito. Generation of 6.6-μm optical parametric oscillation with periodically poled $LiNbO_3$. *Applied Optics*, 38:2560, 1999.

[44] M.A.Watson; M.V.O'Connor; P.S.Lloyd; D.P.Shepherd; D.C.Hanna; C.B.E.Gawith; L.Ming and P.G.R.Smith. Extended operation of synchronously pumped optical parametric oscillators to longer idler wavelengths. *Optics Letters*, 27:2106, 2002.

[45] M.J.McCarthy and D.C.Hanna. All-solid-state synchronously pumped optical parametric oscillator. *Journal of the Optical Society of America .B*, 10:2180, 1993.

[46] J.E.Bjorkholm. Efficient optical parametric oscillation using doubly and singly resonant cavities. *Applied Physics Letters*, 13:53, 1968.

[47] J.E.Bjorkholm. Some spectral properties of doubly and singly resonant pulsed optical parametric oscillators. *Applied Physics Letters*, 13:399, 1968.

[48] H.Kogelnik and T.Li. Laser beams and resonators. *Applied Optics*, 5:1550, 1966.

[49] L.B.Kreuzer. Single mode oscillation of a pulsed singly resonant optical parametric oscillator. *Applied Physics Letters*, 15:263, 1969.

[50] J.E.Bjorkholm. Some effects of spatially nonuniform pumping in pulsed optical parametric oscillators. *IEEE Journal of Quantum Electronics*, 7:109, 1971.

[51] R.W.Wallace. Stable, efficient, optical parametrics oscillaors pumped with doubled Nd:YAG. *Applied Physics Letters*, 17:497, 1970.

[52] D.C.Hanna; B.Luther-Davies and R.C.Smith. Singly resonant proustite parametric oscillator tuned from 1.22 to 8.5 μm. *Applied Physics Letters*, 22:440, 1973.

[53] V.Petrov; F.Rotermund and F.Noack. Generation of high-power femtosecond light pulses at 1 kHz in the mid-infrared spectral range between 3 and 12 μm by second-order nonlinear processes in optical crystals. *Journal of Optics A: Pure and Applied Optics*, 3:1, 2001.

[54] R. Laenen; K. Simeonidis and A. Laubereau. Subpicosecond spectroscopy of liquid water in the infrared: Effect of deuteration on the structural and vibrational dynamics. *Journal of Physical Chemistry*, 106:408, 2002.

[55] G.Richmond. Molecular bonding and interactions at aqueous surfaces as probed by vibrational sum frequency spectroscopy. *Chemical Review*, 102:2693, 2002.

[56] E.C.Cheung and J.M.Liu. Theory of a synchronously pumped optical parametric oscillator in steady-state operation. *Journal of the Optical Scoiety of America B.*, 7:1385, 1990.

[57] E.C.Cheung and J.M.Liu. Efficient generation of ultrashort, wavelength-tunable infrared pulses. *Journal of the Optical Society of America B.*, 8:1491, 1991.

[58] B.Luther-Davies; V.Kolev; M.Lederer; N.Madsen; A.Rode; J.Giesekus; K.Du; M.Duering. Table-top 50-W laser system for ultra-fast laser ablation. *Applied Physics A*, 79:1051, 2004.

[59] L.E.Myers; G. D. Miller; R. C. Eckardt; M. M. Fejer; R. L. Byer; and W. R. Bosenberg. Quasi-phase-matched 1.064-μm-pumped optical parametric oscillator in bulk periodically poled $LiNbO_3$. *Optics Letters*, 20:52, 1995.

[60] M.Yamada; N.Nada; M.Saitoh and k.Watanabe. Yamada - first-order quasi-phase matched $LiNbO_3$ waveguide periodically poled by applying an external field for efficient blue second-harmonic generation. *Applied Physics Letters*, 62:435, 1993.

[61] L.E.Myers. Periodically poled lithium niobate and quasi-phase matched optical parametric oscillators. *IEEE Journal of Quantum Electronics*, 33:1663, 1997.

[62] F.Laurell. Periodically poled materials for miniature light sources. *Optical Materials*, 11:235, 1999.

[63] M.Taya; M.C. Bashaw; and M.M.Fejer. Photorefractive effects in periodically poled ferroelectrics. *Optics Letters*, 21:857, 1996.

[64] L.Arizmendi. Photonic applications of lithium niobate crystals. *Physica Status Solidi*, 201:253, 2004.

[65] L.E.Myers; R. C. Eckardt; M. M. Fejer; R. L. Byer; W. R. Bosenberg and J.W.Pierce. Quasi-phase-matched optical parametric oscillators in bulk periodically poled $LiNbO_3$. *Journal of the Optical Society of America B.*, 12:2102, 1995.

[66] T.R.Volk; N.M.Rubinina and M.Wohlecke. Optical-damage-resistant impurities in lithium niobate. *Journal of the Optical Society of America B.*, 11:1681, 1994.

[67] E.P.Kokanyan; V.G.Babajanyan; G.G.Demirkhanyan; J.B.Gruber and S.Erdei. Periodically poled structures in doped lithium niobate crystals. *Journal of Applied Physics*, 92:1544, 2002.

[68] P.F.Bordui and M.M.Fejer. Inorganic crystals for nonlinear optical frequency conversion. *Annual Review of Materials Science*, 23:321, 1993.

[69] Y.Furukawa; K.Kitamura and S.Takekawa. Stoichiometric MgO:$LiNbO_3$ as an effective material for nonlinear optics. *Optics Letters*, 23:1892, 1998.

[70] D.H.Jundt. Temperature-dependent sellmeier equation for the index of refraction, n_e, in congruent lithium niobate. *Optics Letters*, 22:1553, 1997.

[71] D.E.Zelmon; D.L.Small and D.Jundt. Infrared corrected sellmeier coefficients for congruently grown lithium niobate and 5 mol. % magnesium oxide-doped lithium niobate. *Journal of the Optical Society of America B.*, 14:3319, 1997.

[72] H.Y.Shen; H.Xu; Z.D.Zeng; W.X.Lin; R.F.Wu; and G. F. Xu. Measurement of refractive indices and thermal refractive-index coefficients of $LiNbO_3$ crystal doped with 5 mol. % MgO. *Applied Optics*, 31:6695, 1992.

[73] A.Piskarskas; V.Smilgevicius; A.Umbrass. Continuous parametric generation of picosecond light pulses. *Soviet Journal of Quantum Electronics*, 18:155, 1988.

[74] H.Giordano. *Development of a high-power ultrashort pulse duration Optical Amplification System.* PhD Thesis, submitted at ANU, 1998.